# Modeling and simulation of laser shock waves in elasto-plastic 1D layered specimens

L. Lapostolle *, K. Derrien, L. Morin, L. Berthe, O. Castelnau

*PIMM, Arts et Metiers Institute of Technology, CNRS, Cnam, HESAM University, 151 boulevard de l'Hopital, 75013 Paris, France*

A B S T R A C T

The aim of this paper is to study the effect of microstructure heterogeneity upon elasto-plastic wave propagation generated during laser shot peening. We consider a simplified elasto-plastic laminate specimen subjected to uniaxial strain. The microstructure is composed of two phases alternating periodically and perfectly bonded together. The associated PDE system is solved using a high-resolution Godunov scheme, allowing to study the wave propagation in the heterogeneous structure. It is found that, even for a small mechanical contrast between the two phases, the considered laminate microstructure has a significant effect on the distribution of plastic strain. In addition, an elasto-plastic homogenization of the laminate has been carried out, and the resulting Homogeneous Equivalent Medium (HEM) has been used to decrease the computation time of the wave propagation. The HEM-based model is able to reproduce accurately the full-field solution in terms of distribution of mean plastic strain within the specimen and its fluctuation between the two phases.

## 1. Introduction

The mechanical process motivating this work is Laser Shot Peening (LSP). The process consists in impacting the surface of a metallic target with a high intensity laser beam (>GW/cm$^2$), producing a high pressure plasma in the GPa range. In reaction, a shock wave travels through the specimen and generates plastic strain, as illustrated in Fig. 1a. Upon relaxation, this induces compressive residual stresses in the specimen. Those residual stresses have been shown to increase the fatigue resistance of the specimen treated (Peyre et al., 1996, 1998; Ding and Ye, 2006). In the standard experimental configuration, the interaction is confined by water (Fox, 1974) allowing better efficiency. A protective coating can be used to avoid strong thermal effects inducing tensile stresses at the uppermost surface. In this configuration, the profile pressure of the plasma typically lasts a few tens of nanoseconds and has been modeled in several works (Fabbro et al., 1990; Peyre et al., 2007, 2012; Rondepierre et al., 2021). A typical profile of the plasma pressure, normalized with the maximal pressure, is shown in Fig. 1b. LSP finds applications in the aeronautics industry, as well as in the energy industry, where numerous parts and machines can benefit from fatigue protection treatments (Clauer, 2019; Montross et al., 2002).

The analytical and numerical modeling of LSP has been studied over the years, starting with the seminal works of Ballard (1991) and Braisted (1999). The principle is to simulate the propagation of elasto-plastic waves that are produced by dynamic stress impulse. In most of the works, the impacted specimens are assumed to be homogeneous and to exhibit an isotropic mechanical behavior, with an elastic behavior described by the equation of state (EOS) (Peyre et al., 2003, 2012) when necessary, or with a purely elastic behavior (Song, 2010). In terms of plastic properties, the most used model at high strain rates is the Johnson–Cook model (Johnson and Cook, 1983). Other authors also investigated the effect of LSP on single crystals (Wang et al., 2008; Vukelic et al., 2009) and bi-crystals (Vukelić et al., 2009) both experimentally and numerically, using crystal plasticity based constitutive equations. Residual stresses are then calculated from the residual plastic strain field generated by the plastic wave propagation. Several process conditions can be explored using numerical simulations such as the overlapping of many laser pulses (Brockman et al., 2012; Chaieb, 2004).

LSP processing usually involves large spot size of a few millimeters together with a high power laser source, to achieve the desired plasma pressures. An interesting alternative is to consider a low laser energy, so that the whole system can be more compact and transported by an optical fiber, which is known as *micro-LSP*. The consequence of a low laser energy is a decrease of the laser spot sizes, which can become close to the grain size for some materials (for instance aluminum alloys). Therefore, studying the interactions between the shock wave and the microstructure thus becomes needed when the laser spot diameter is small, such as in micro-LSP. On top of that, one can anticipate that

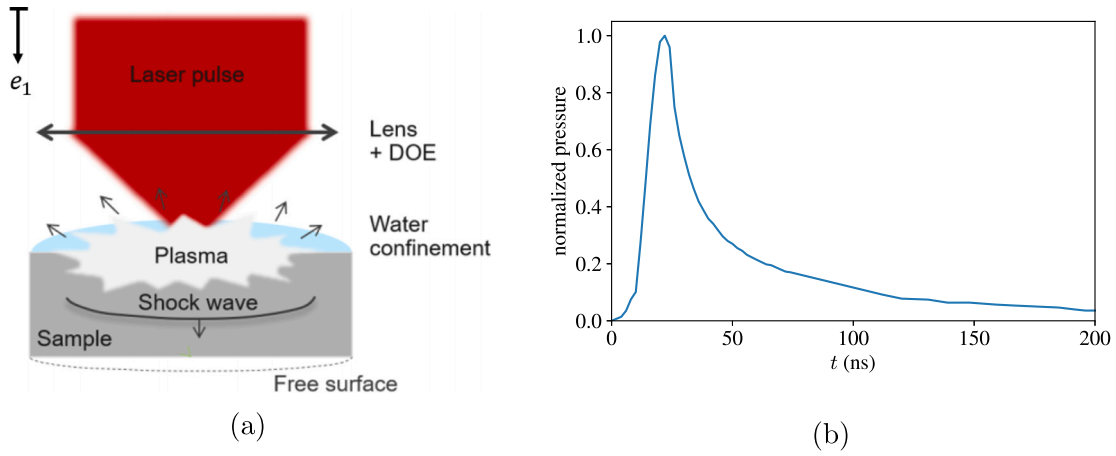


**Fig. 1.** Laser shot peening processing. (a) Representation of the LSP process (after (Scius-Bertrand et al., 2021)). (b) Typical profile of the normalized pressure at the center of the impact (Le Bras et al., 2019).

accounting for the elongated grain shape and/or non-random distribution of the grain orientations, very often encountered in most industrial alloys (and known as morphological and crystallographic textures in the literature), is a prerequisite to improve the control of the effect of LSP. Hence, the problem to be addressed is the propagation of a stress wave in a heterogeneous (polycrystalline) elasto-plastic specimen. Although the propagation of elastic stress waves in heterogeneous media has been widely studied (Berezovski et al., 2006; Tedesco and Landis, 1989), especially for seismology applications, the numerical study of elasto-plastic shockwaves in heterogeneous media is scarce (Agrawal and Bhattacharya, 2014; Chen et al., 2004; Chen and Chandra, 2004 focused mostly on shockwaves with no plastic effects). Due to the non-linearities brought by plasticity, the numerical simulation of stress waves in heterogeneous materials requires notably specific numerical solvers for hyperbolic equations that do not induce spurious oscillations nor damping.

From the modeling point of view, the up-scaling of elasto-plastic heterogeneous media under dynamic conditions is also of interest in order to decrease the computational time of full-field simulations (inherent to the spatial description of the heterogeneities). Under quasi-static conditions, the overall elastic behavior of a heterogeneous material can be usually determined from the description of its local constituents using homogenization techniques (Milton, 2002). Several works have been proposed to enrich homogenization techniques. In presence of dynamic effects, the homogenized wave equation has been studied by mean of a spatial filter that allows to separate scales in the heterogeneity pattern of the medium (Capdeville et al., 2010; Capdeville and Marigo, 2007). On the other hand, analytic models have been derived to extent homogenization scheme to plasticity (but in quasi-static conditions) for ideal laminate microstructures (Chatzigeorgiou et al., 2009; He and Feng, 2012). However, in presence of both *dynamic* and *plasticity* effects, homogenization techniques are yet to be developed.

The aim of this paper is to study numerically the propagation of a shock wave in an elasto-plastic heterogeneous specimen, in order to assess the effect of microstructure on residual plastic strain distributions. To do so, we will consider the case of a laminate specimen subjected to a uniaxial strain state. This allows to study numerically the effect of a microstructure upon the elasto-plastic wave propagation (and residual plastic strain field). Furthermore, as those full-field simulations can be demanding in terms of computational time, an approximate HEM-based model, based on the quasi-static solution of the elasto-plastic laminate, will also be presented to address the effect of material heterogeneity. Although LSP is motivating this work, the proposed modeling is also valid for various impact problems causing a stress wave to propagate in a material. Mention has to be made to the work of Zhuang et al. (2003) who studied experimentally the propagation of stress waves induced by a plate impact in a layered specimen, reporting a viscous macroscopic behavior due to the laminate nature of the specimen.

The paper is organized as follows. In Section 2, we define the general mechanical framework for a heterogeneous laminate specimen, which we will then use to model the stress wave propagation. In Section 3, we develop an elasto-plastic HEM-based model based on quasi-static loading conditions. Finally, in Section 4, we investigate the propagation of shock wave in laminate elasto-plastic specimens, using both full-field and HEM-based descriptions.

## 2. Mechanical modeling of stress waves in a layered specimen

### 2.1. Equations of elasto-plastic dynamics

LSP introduces, by the way of a high-pressure plasma produced by a laser, stress waves within the specimen. The (local) mechanical behavior of the target material is supposed to be elasto-plastic and obeys the following dynamic equations:

$$\begin{cases} \mathbf{div}(\boldsymbol{\sigma}) = \rho \dfrac{\partial^2 \boldsymbol{u}}{\partial t^2} & \text{Balance of linear momentum} \\ \boldsymbol{\sigma} = \mathbb{C} : \boldsymbol{\varepsilon}_e = \mathbb{C} : \left(\boldsymbol{\varepsilon} - \boldsymbol{\varepsilon}_p\right) & \text{Elastic behavior} \\ \boldsymbol{\varepsilon}(\boldsymbol{u}) = \dfrac{1}{2}(\nabla \boldsymbol{u} + \nabla^{\mathrm{T}} \boldsymbol{u}) & \text{Strain–displacement relation} \\ g = J_2\left(\boldsymbol{\sigma} - \mathbf{X}\right) - R\left(p\right) \leq 0 & \text{Plasticity criterion} \\ \begin{cases} \dot{\boldsymbol{\varepsilon}}_p = \dot{\lambda} \dfrac{\partial g}{\partial \boldsymbol{\sigma}} \\ \dot{\lambda} \geq 0 \\ \dot{\lambda} g = 0, \end{cases} & \text{Flow rule and consistency conditions} \end{cases} \tag{1}$$

where the unknowns are the stress tensor $\boldsymbol{\sigma}$, the plastic strain tensor $\boldsymbol{\varepsilon}_p$ and the displacement field $\boldsymbol{u}$. In system (1), $\boldsymbol{\varepsilon}_e$ is the elastic strain tensor, $\rho$ is the local density, $\mathbb{C}$ is the local stiffness tensor, $g$ is the yield function of plasticity, $\mathbf{X}$ is the backstress (used for kinematic hardening), $R$ is the isotropic hardening function, $p$ is the accumulated plastic strain and $\dot{\lambda}$ is the plastic multiplier. We assume that the plasticity criterion is isotropic where $J_2$ is given by

$$J_2(\boldsymbol{\sigma}) = \sqrt{\frac{3}{2}\left(\boldsymbol{\sigma} - \frac{1}{3}\mathrm{Tr}(\boldsymbol{\sigma})\boldsymbol{I}\right) : \left(\boldsymbol{\sigma} - \frac{1}{3}\mathrm{Tr}(\boldsymbol{\sigma})\boldsymbol{I}\right)}, \tag{2}$$

where $\boldsymbol{I}$ is the second-order identity tensor.

Few remarks concerning the modeling hypotheses of the material behavior can be discussed shortly. In this work, both strain rate effects and "elastic shock behavior" of the material will be neglected. As presented by Seddik et al. (2021), considering a strain rate dependent model acts as a refinement of an elastic perfectly plastic model, and permits to fit more accurately the experimental results. According to their work, an elastic perfectly plastic model already captures the

important features of the propagation. Then, a standard elasticity law is considered, instead of shock Equations Of States (EOS). EOS describe the propagation of the shock when the material's behavior become dependent on the applied pressure, which results in different wave speeds at various locations of the wave. Moreover, it has been shown that the effect of EOS on plastic strain and residual stress fields is generally negligible (Chaieb, 2004). Therefore, following the analysis of Ballard (1991) who defines applied pressure thresholds based on the material properties under which the material's behavior can be assumed not to be hydrodynamic, we choose to neglect the shock behavior, and we will check the validity of his hypothesis for our applications.

### 2.2. Uniaxial case

As mentioned in the introduction, we aim at investigating the effect of a microstructure upon elasto-plastic wave propagation. We consider in this paper the simplified case of a *layered specimen* which allows to investigate the main features of LSP in one dimension. The following 1d ansatz is thus considered:

(1) *Hypotheses on the mechanical properties.* In terms of description of the microstructure, we assume that the spatial domain is divided into a large number of layers, each one behaving with its own local mechanical behavior. Anticipating the developments to come, the choice is now made to consider a periodic microstructure made of two phases of volume fraction $f_1$ and $f_2$ respectively. This corresponds to a composite material with a periodic repetition of layers with mechanical properties varying from one to another, as represented in Fig. 2. Finally we assume that the interface between the layers is perfect. The mechanical property fields thus only depend on the variable $x_1$:

$$\rho = \rho(x_1), \quad \mathbb{C} = \mathbb{C}(x_1), \quad \sigma_Y = \sigma_Y(x_1). \tag{3}$$

The elastic behavior of the local phases will be assumed to be isotropic, so that the whole problem exhibits transverse isotropy. In this case, the stiffness tensor $\mathbb{C}$ reduces to

$$\mathbb{C}(x_1) = 3\kappa(x_1)\mathbb{J} + 2\mu(x_1)\mathbb{K}, \tag{4}$$

where $\kappa$ and $\mu$ are respectively the bulk and shear moduli, and $\mathbb{J}$ and $\mathbb{K}$ are fourth-order tensors defined as

$$\mathbb{J} = \frac{1}{3}\boldsymbol{I}\otimes\boldsymbol{I} \quad \text{and} \quad \mathbb{K} = \mathbb{I} - \mathbb{J}, \tag{5}$$

with $\boldsymbol{I}$ the second-order identity tensor and $\mathbb{I}$ the fourth-order identity tensor. The 2-indices matrix representation (using Kelvin convention, see e.g. Morin et al. (2020)) of the stiffness tensor reads:

$$\mathbb{C}(x_1) = \begin{pmatrix} C_{1111}(x_1) & C_{1122}(x_1) & C_{1122}(x_1) & 0 & 0 & 0 \\ C_{1122}(x_1) & C_{1111}(x_1) & C_{1122}(x_1) & 0 & 0 & 0 \\ C_{1122}(x_1) & C_{1122}(x_1) & C_{1111}(x_1) & 0 & 0 & 0 \\ 0 & 0 & 0 & 2C_{1212}(x_1) & 0 & 0 \\ 0 & 0 & 0 & 0 & 2C_{1212}(x_1) & 0 \\ 0 & 0 & 0 & 0 & 0 & 2C_{1212}(x_1) \end{pmatrix}, \tag{6}$$

with $2C_{1212}(x_1) = C_{1111}(x_1) - C_{1122}(x_1) = 2\mu(x_1)$ and $C_{1122}(x_1) = \kappa(x_1) - 2\mu(x_1)/3$. In order to unify the notations during the forthcoming developments, the $C_{ijkl}$ coefficients will be used in all calculations.

(2) *Hypotheses on the plasticity model.* An elastic perfectly plastic model will be assumed for the sake of simplicity. The backstress $\boldsymbol{X}$ is thus supposed to vanish and the yield limit $R(p)$ is taken as constant.

$$\boldsymbol{X} = \boldsymbol{0} \quad \text{and} \quad R(p) = \sigma_Y, \tag{7}$$

where $\sigma_Y$ is the (local) yield strength.

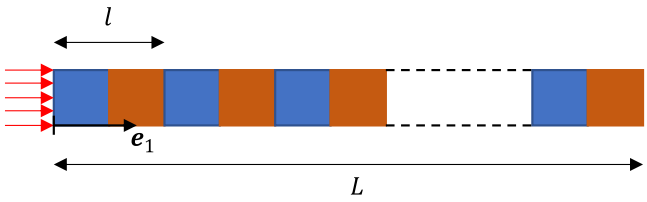


**Fig. 2.** Representation of the layered specimen. The plasma pressure is applied to the left on the specimen of length $L$ and comprising many layers. Direction $\boldsymbol{e}_1$ denotes the direction of 1D wave propagation.

(3) *Hypotheses on the mechanical fields.* The mechanical fields are supposed to be axisymmetric with respect to the propagation axis, denoted by $\boldsymbol{e}_1$. This choice is mostly motivated by the fact that the laser used in experimental conditions has a circular spot, applied at the center of the specimen. Moreover, we consider that these fields only depend on one spatial dimension corresponding to the axis of symmetry $\boldsymbol{e}_1$ (in addition to their time dependence $t$), i.e. all gradients with respect to $x_2$ and $x_3$ vanish, and that the specimen exhibits a transverse isotropic mechanical behavior. The strain tensor is supposed to be uniaxial, along the direction $\boldsymbol{e}_1$. This hypothesis, which follows the previous work of Ballard (1991), is reasonable provided that the duration of impacts is short (e.g. less than a few hundreds of nanoseconds for a steel material). In doing so however, we lose the description of the propagation of radial waves, and the description of the state of the material close to the edge of the laser spot, which can be the locus for important shear stresses. These specific issues are left for future works. The displacement field $\boldsymbol{u}$ and total strain tensor $\boldsymbol{\varepsilon}$ are thus supposed to be of the form

$$\boldsymbol{u} = u_1(x_1,t)\boldsymbol{e}_1, \quad \boldsymbol{\varepsilon} = \varepsilon_{11}(x_1,t)\boldsymbol{e}_1\otimes\boldsymbol{e}_1, \tag{8}$$

where $\varepsilon_{11} = \partial u_1/\partial x_1$, and $x_1$ the coordinate along $\boldsymbol{e}_1$. Moreover we make the (standard) hypothesis that plasticity is incompressible so that the plastic strain tensor $\boldsymbol{\varepsilon}^p$ is of the form

$$\boldsymbol{\varepsilon}_p = \varepsilon_{p,11}(x_1,t)\left(\boldsymbol{e}_1\otimes\boldsymbol{e}_1 - \frac{1}{2}\boldsymbol{e}_2\otimes\boldsymbol{e}_2 - \frac{1}{2}\boldsymbol{e}_3\otimes\boldsymbol{e}_3\right). \tag{9}$$

By material symmetry and the form of $\boldsymbol{\varepsilon}$ given in (8), the form of the stress tensor $\boldsymbol{\sigma}$ is

$$\boldsymbol{\sigma} = \sigma_{11}(x_1,t)\boldsymbol{e}_1\otimes\boldsymbol{e}_1 + \sigma_{22}(x_1,t)\left(\boldsymbol{e}_2\otimes\boldsymbol{e}_2 + \boldsymbol{e}_3\otimes\boldsymbol{e}_3\right). \tag{10}$$

To summarize, we have now the following expressions for $\sigma_{11}$, $\sigma_{22}$ and $J_2(\boldsymbol{\sigma})$:

$$\begin{aligned} &\sigma_{11} = C_{1111}\varepsilon_{11} + \left(C_{1122} - C_{1111}\right)\varepsilon_{p,11}, \\ &\sigma_{22} = \sigma_{33} = C_{1122}\varepsilon_{11} + \frac{C_{1111} - C_{1122}}{2}\varepsilon_{p,11}, \\ &J_2(\boldsymbol{\sigma}) = |\sigma_{11} - \sigma_{22}|. \end{aligned} \tag{11}$$

### 2.3. Stress wave propagation equation

Using the previous hypotheses, the stress wave propagation equations can be presented during elastic propagation and plastic propagation for this simplified 1d problem.

#### 2.3.1. Elastic propagation

First, we assume that the material response is purely elastic, so that $\dot{\boldsymbol{\varepsilon}}_p = 0$. Since the mechanical fields depend spatially only on the variable $x_1$, the first two equations of system (1) lead to the partial derivative system

$$\begin{cases} \dfrac{\partial\sigma_{11}}{\partial x_1}(x_1,t) = \rho(x_1)\dfrac{\partial v_1}{\partial t}(x_1,t) \\ \dfrac{\partial\sigma_{11}}{\partial t}(x_1,t) = C_{1111}(x_1)\dfrac{\partial v_1}{\partial x_1}(x_1,t), \end{cases} \tag{12}$$

where $v_1$ is the material velocity, defined as $v_1 = \partial u_1/\partial t$. The system (12) can be cast under the following matrix form:

$$\boldsymbol{U}_t + \boldsymbol{A}\cdot\boldsymbol{U}_{x_1} = \boldsymbol{0}, \tag{13}$$

where the partial derivatives are denoted by the subscripts $x_1$ and $t$. In Eq. (13), $\boldsymbol{U}$ and $\boldsymbol{A}$ are given by

$$\boldsymbol{U} = \begin{pmatrix}\sigma_{11}\\ v_1\end{pmatrix}, \qquad \boldsymbol{A} = \begin{pmatrix}0 & -C_{1111}\\ -\dfrac{1}{\rho} & 0\end{pmatrix}. \tag{14}$$

Eq. (13) is known as the advection equation, and describes the propagation of stress waves. The matrix $\boldsymbol{A}$ has two eigenvalues, both corresponding, in absolute value, to the axial wave velocity in the material:

$$c(x_1) = \sqrt{\frac{C_{1111}(x_1)}{\rho(x_1)}}. \tag{15}$$

It is worth noting that this propagation problem can be written alternatively by considering the sole displacement as the unknown. This would lead to the wave equation for the displacement $u_1$:

$$\frac{C_{1111}(x_1)}{\rho(x_1)}\frac{\partial^2 u_1}{\partial x_1^2} = \frac{\partial^2 u_1}{\partial t^2}. \tag{16}$$

The physical phenomenon described by Eq. (16) is the same as for Eq. (13), but the unknown is different. Though mathematically equivalent, both equations cannot be solved by the same numerical methods. The resolution of Eq. (16) can be subject to numerical artifacts, as it will be discussed in Section 4.1.

#### 2.3.2. Plastic propagation

In the case of a plastic behavior, the plastic strain increment $\dot{\boldsymbol{\epsilon}}_p$ is non zero. Together with the assumption of axisymmetry of the stress tensor, the incremental form of the plasticity criterion leads to an explicit relation between the longitudinal plastic strain rate $\dot{\epsilon}_{p,11}$ and the rate of total strain $\dot{\epsilon}_{11} = \partial v_1/\partial x_1$:

$$\dot{\epsilon}_{p,11} = \alpha\dot{\epsilon}_{11} = \alpha\frac{\partial v_1}{\partial x_1}, \tag{17}$$

where $\alpha$ is given in our case by:

$$\alpha = \frac{2}{3}. \tag{18}$$

The incremental form of the plasticity criterion reads:

$$\dot{J}_2(\boldsymbol{\sigma}) = 0. \tag{19}$$

Consequently, considering (8), (9) and (11), the elasto-plastic propagation equations reduce, for the ansatz considered, to

$$\begin{cases}\dfrac{\partial\sigma_{11}}{\partial x_1} = \rho\dfrac{\partial v_1}{\partial t}\\ \dfrac{\partial\sigma_{11}}{\partial t} = \left(C_{1111}(1-\alpha) + \alpha C_{1122}\right)\dfrac{\partial v_1}{\partial x_1}.\end{cases} \tag{20}$$

As in the elastic case, this system can be written under the matrix form (13), where $\boldsymbol{U}$ and $\boldsymbol{A}$ are this time given by

$$\boldsymbol{U} = \begin{pmatrix}\sigma_{11}\\ v_1\end{pmatrix}, \qquad \boldsymbol{A} = \begin{pmatrix}0 & C_{1111}(\alpha-1) - \alpha C_{1122}\\ -\dfrac{1}{\rho} & 0\end{pmatrix}. \tag{21}$$

The resolution of this system permits to determine the stress increment $\dot{\sigma}_{11}$ which allows the determination of the axial strain increment $\dot{\epsilon}_{11}$ using Eq. $(20)_2$ and ultimately the determination of $\dot{\epsilon}_{p,11}$ using Eq. (17).

## 3. Elasto-plastic homogenization of laminate specimen for static loading

The aim of this section is to derive an elasto-plastic HEM-based model of the laminate microstructure considered in Section 2. We consider the case where the two phases share the same density $\rho$. Thus, instead of homogenizing the wave equation with an elasto-plastic behavior of the phases (as it was done by Capdeville et al. (2010) in elasticity solely, with the definition of an effective density $\widetilde{\rho} = \langle\rho\rangle$, where $\langle\cdot\rangle$ is the spatial average operator defined by Eq. (24)) we will consider the homogenization of the laminate microstructure in *quasi-static conditions*, following previous work (Chatzigeorgiou et al., 2009; He and Feng, 2012). This will permit to define the HEM-based elasto-plastic behavior of the laminate specimen, whose behavior depends on several internal parameters related to its microstructure, which will then be used in the wave propagation equation.

We begin with the determination of the effective stiffness and plastic strain tensors, for a given initial mechanical state.

### 3.1. Effective stiffness tensor

The effective elastic constitutive relation reads

$$\overline{\boldsymbol{\sigma}} = \widetilde{\mathbb{C}} : \widetilde{\boldsymbol{\epsilon}}_e, \tag{22}$$

where $\widetilde{\mathbb{C}}$ is the (unknown) effective stiffness tensor, $\overline{\boldsymbol{\sigma}}$ is the macroscopic stress tensor and $\widetilde{\boldsymbol{\epsilon}}_e$ is the effective elastic strain tensor. The macroscopic stress $\overline{\boldsymbol{\sigma}}$ and strain $\overline{\boldsymbol{\epsilon}}$ are defined by

$$\overline{\boldsymbol{\sigma}} = \langle\boldsymbol{\sigma}\rangle, \quad \overline{\boldsymbol{\epsilon}} = \langle\boldsymbol{\epsilon}\rangle. \tag{23}$$

In Eq. (23), the operator $\langle\cdot\rangle$ is the spatial average over the domain $V$ defined by

$$\langle f\rangle = \frac{1}{\mathrm{vol}(V)}\int_V f\,\mathrm{d}V. \tag{24}$$

In order to determine the stiffness tensor $\widetilde{\mathbb{C}}$ we make use of (standard) properties of laminated specimens, that is the uniformity of the axial stress and in-plain elastic strain:

$$\sigma_{11} = \overline{\sigma}_{11}, \quad \sigma_{12} = \overline{\sigma}_{12}, \quad \sigma_{13} = \overline{\sigma}_{13}, \quad \varepsilon_{22} = \overline{\varepsilon}_{22}, \quad \varepsilon_{33} = \overline{\varepsilon}_{33}, \quad \varepsilon_{23} = \overline{\varepsilon}_{23}, \tag{25}$$

as well as the per-phase homogeneous stress and strain states in both phases, which are exact properties also valid when the phases deform plastically as considered in the next section (Postma, 1955; Milton, 2002; He and Feng, 2012). Those relations lead to the definition of the effective stiffness tensor, which describes a transverse isotropic behavior by material symmetry. Using Kelvin's notation, $\widetilde{\mathbb{C}}$ reads

$$\widetilde{\mathbb{C}} = \begin{pmatrix}\widetilde{C}_{1111} & \widetilde{C}_{1122} & \widetilde{C}_{1122} & 0 & 0 & 0\\ \widetilde{C}_{1122} & \widetilde{C}_{2222} & \widetilde{C}_{2233} & 0 & 0 & 0\\ \widetilde{C}_{1122} & \widetilde{C}_{2233} & \widetilde{C}_{2222} & 0 & 0 & 0\\ 0 & 0 & 0 & 2\widetilde{C}_{2323} & 0 & 0\\ 0 & 0 & 0 & 0 & 2\widetilde{C}_{1313} & 0\\ 0 & 0 & 0 & 0 & 0 & 2\widetilde{C}_{1313}\end{pmatrix}, \tag{26}$$

where the non-null components are given by[1]

$$\begin{aligned}
\widetilde{C}_{1111} &= \left\langle\frac{1}{C_{1111}}\right\rangle^{-1},\\
\widetilde{C}_{2222} &= \langle C_{1111}\rangle + \left\langle\frac{1}{C_{1111}}\right\rangle^{-1}\left\langle\frac{C_{1122}}{C_{1111}}\right\rangle^2 - \left\langle\frac{C_{1122}^2}{C_{1111}}\right\rangle,\\
\widetilde{C}_{1122} &= \left\langle\frac{1}{C_{1111}}\right\rangle^{-1}\left\langle\frac{C_{1122}}{C_{1111}}\right\rangle,\\
\widetilde{C}_{2233} &= \langle C_{1122}\rangle + \left\langle\frac{1}{C_{1111}}\right\rangle^{-1}\left\langle\frac{C_{1122}}{C_{1111}}\right\rangle^2 - \left\langle\frac{C_{1122}^2}{C_{1111}}\right\rangle,\\
\widetilde{C}_{1313} &= \left\langle\frac{1}{C_{1212}}\right\rangle^{-1}, \quad 2\widetilde{C}_{2323} = 2\langle C_{1212}\rangle = \widetilde{C}_{2222} - \widetilde{C}_{2233}.
\end{aligned} \tag{27}$$

[1] The details of the calculations leading to the definition of the effective stiffness tensor are given in Appendix A.

### 3.2. Effective plastic strain tensor

Now that the effective stiffness tensor has been derived, we are looking for the expression of the effective plastic strain tensor $\widetilde{\boldsymbol{\varepsilon}}_p$ in order that it verifies

$$\overline{\boldsymbol{\sigma}} = \widetilde{\mathbb{C}} : \left(\overline{\boldsymbol{\varepsilon}} - \widetilde{\boldsymbol{\varepsilon}}_p\right) = \left\langle \mathbb{C} : \left(\boldsymbol{\varepsilon} - \boldsymbol{\varepsilon}_p\right)\right\rangle, \quad \text{and} \quad \widetilde{\boldsymbol{\varepsilon}}_e = \overline{\boldsymbol{\varepsilon}} - \widetilde{\boldsymbol{\varepsilon}}_p. \tag{28}$$

We remind here that local plasticity is incompressible (i.e. the trace of the local plastic strain tensor vanishes). Let us first detail the expression of the local strain $\varepsilon_{11}$ and stress $\sigma_{22}$ (which also verifies $\sigma_{22} = \sigma_{33}$):

$$\begin{cases} \varepsilon_{11} = \dfrac{1}{C_{1111}}\sigma_{11} - \varepsilon_{p,11}\left(\dfrac{C_{1122}}{C_{1111}} - 1\right) \\ \sigma_{22} = C_{1122}\varepsilon_{11} + \varepsilon_{p,11}\dfrac{C_{1111} - C_{1122}}{2}. \end{cases} \tag{29}$$

Injecting the first equation of (29) into the second one, and taking the average value of both equations leads to the following system:

$$\begin{cases} \overline{\varepsilon}_{11} = \left\langle \dfrac{1}{C_{1111}} \right\rangle \overline{\sigma}_{11} - \left\langle \varepsilon_{p,11}\left(\dfrac{C_{1122}}{C_{1111}} - 1\right)\right\rangle \\ \overline{\sigma}_{22} = \left\langle \dfrac{C_{1122}}{C_{1111}} \right\rangle \overline{\sigma}_{11} + \left\langle \varepsilon_{p,11}\left(\dfrac{C_{1122} + C_{1111}}{2} - \dfrac{C_{1122}^2}{C_{1111}}\right)\right\rangle. \end{cases} \tag{30}$$

Then, we define the intermediate dimensionless quantities

$$\begin{aligned} M_1 &= \left\langle \varepsilon_{p,11}\left(\frac{C_{1122}}{C_{1111}} - 1\right)\right\rangle \quad \text{and} \\ M_2 &= \frac{1}{\widetilde{C}_{1122}}\left\langle \varepsilon_{p,11}\left(\frac{C_{1111} + C_{1122}}{2} - \frac{C_{1122}^2}{C_{1111}}\right)\right\rangle, \end{aligned} \tag{31}$$

which will be useful to link the local plastic strain to the effective plastic strain. The system (30) is now recast so as to separate the stress and the strains:

$$\begin{cases} \overline{\sigma}_{11} = \widetilde{C}_{1111}\overline{\varepsilon}_{11} + \widetilde{C}_{1111}M_1 \\ \overline{\sigma}_{22} = \widetilde{C}_{1122}\overline{\varepsilon}_{11} + \widetilde{C}_{1122}(M_1 + M_2). \end{cases} \tag{32}$$

It is then straightforward to identity the non-null components of the effective plastic strain from Eq. (32):

$$\begin{cases} \widetilde{\varepsilon}_{p,11} = -M_1 + \dfrac{2\widetilde{C}_{1122}^2}{\widetilde{C}_{1111}\left(\widetilde{C}_{2222} + \widetilde{C}_{2233}\right) - 2\widetilde{C}_{1122}^2}M_2 \\ \widetilde{\varepsilon}_{p,22} = \widetilde{\varepsilon}_{p,33} = \dfrac{\widetilde{C}_{1111}\widetilde{C}_{1122}}{2\widetilde{C}_{1122}^2 - \widetilde{C}_{1111}\left(\widetilde{C}_{2222} + \widetilde{C}_{2233}\right)}M_2. \end{cases} \tag{33}$$

Some comments are in order:

- Unlike the macroscopic stress and total strains, the effective plastic strain is not defined by averaging the local corresponding quantity, i.e $\widetilde{\boldsymbol{\varepsilon}}_p \neq \langle \boldsymbol{\varepsilon}_p \rangle$, which is a standard property in elasto-plastic homogenization (He and Feng, 2012; Chatzigeorgiou et al., 2009).
- The effective plastic strain is not incompressible ($\mathrm{Tr}\left(\widetilde{\boldsymbol{\varepsilon}}_p\right) \neq 0$) in contrast with the local plastic strain which verifies the property of incompressibility ($\mathrm{Tr}\left(\boldsymbol{\varepsilon}_p\right) = 0$). This comes from the fact that when local plastic strains come in play, an elastic strain field is generated in order to accommodate the plastic incompatibilities.

### 3.3. Effective incremental elasto-plastic behavior

Then the next step is to derive the effective incremental elasto-plastic behavior. The quantities we are ultimately looking for are thus $\partial\overline{\sigma}_{11}/\partial\overline{\varepsilon}_{11}$ and $\partial\overline{\sigma}_{22}/\partial\overline{\varepsilon}_{11}$. Their expression will depend on the local elasto-plastic behavior of the phase. In the following, the index $(i)$ indicates that a quantity is evaluated in the phase $(i)$.

First, we remind that the local axial plastic strain rate $\dot{\varepsilon}_{p,11}^{(i)}$ (when it is non-null) can be deduced from the local total strain $\dot{\varepsilon}_{11}^{(i)}$ rate by the relation (17)

$$\dot{\varepsilon}_{p,11}^{(i)} = \alpha^{(i)}\dot{\varepsilon}_{11}^{(i)}, \tag{34}$$

where $\alpha^{(i)}$ is defined according to Eq. (18). Then, by taking advantage of the relation $\dot{\sigma}_{11}^{(1)} = \dot{\sigma}_{11}^{(2)}$, which is valid for a quasi-static loading, it is possible to express the local total strains rate $\dot{\varepsilon}^{(i)}$ as a function of the total macroscopic strain rate $\dot{\overline{\varepsilon}}_{11}$ by the relation

$$\dot{\varepsilon}_{11}^{(i)} = \beta^{(i)}\dot{\overline{\varepsilon}}_{11}, \tag{35}$$

where the coefficients $\beta^{(i)}$, which are components of a strain-rate localization tensor, remain to be found.

It is straightforward to note that, from system (32) in incremental form and Eqs. (31), (34) and (35), the expressions of $\dot{\overline{\sigma}}_{11}$ and $\dot{\overline{\sigma}}_{22}$ depend solely on $\dot{\overline{\varepsilon}}_{11}$ and $\dot{\varepsilon}_{p,11}^{(i)}$. From such relations one can easily identify the values of $\partial\overline{\sigma}_{11}/\partial\overline{\varepsilon}_{11}$ and $\partial\overline{\sigma}_{22}/\partial\overline{\varepsilon}_{11}$, which can in turn be used to properly define the advection equation. Thus, the determination of the conditions promoting local plasticity together with the values of the parameters $\beta^{(i)}$ suffices to define completely the incremental elasto-plastic behavior.

Several cases need to be considered, depending on which phase reaches (or not) plasticity. First, we introduce the quantities $\overline{\sigma}^{(+)}$ and $\overline{\sigma}^{(-)}$, which correspond to the values of $\overline{\sigma}_{11}$ for which one of the phases starts to reach plasticity, when $\dot{\overline{\varepsilon}}_{11} > 0$ and $\dot{\overline{\varepsilon}}_{11} < 0$, respectively. Their expressions are obtained by expressing the yield criterion (1) with local stresses given by (11) while noting that $\sigma_{11}^{(i)} = \bar{\sigma}_{11}$ (see (B.5)):

$$\begin{cases} \overline{\sigma}^{(+)} = \min\limits_{(i)}\left(\dfrac{C_{1111}^{(i)}}{C_{1111}^{(i)} - C_{1122}^{(i)}}\left[\sigma_Y^{(i)} - \left(\dfrac{(C_{1122}^{(i)})^2}{C_{1111}^{(i)}} - \dfrac{C_{1111}^{(i)} + C_{1122}^{(i)}}{2}\right)\varepsilon_{p,11}^{(i)}\right]\right) \\ \overline{\sigma}^{(-)} = \max\limits_{(i)}\left(\dfrac{C_{1111}^{(i)}}{C_{1111}^{(i)} - C_{1122}^{(i)}}\left[-\sigma_Y^{(i)} - \left(\dfrac{(C_{1122}^{(i)})^2}{C_{1111}^{(i)}} - \dfrac{C_{1111}^{(i)} + C_{1122}^{(i)}}{2}\right)\varepsilon_{p,11}^{(i)}\right]\right). \end{cases} \tag{36}$$

With $\overline{\sigma}^{(+)}$ and $\overline{\sigma}^{(-)}$, only $\overline{\sigma}_{11}$ is in fact required to assess whether one of the phases started to plastify. However to follow the form of the local plasticity criterion, this assessment will be expressed as a condition on $\overline{\sigma}_{11} - \overline{\sigma}_{22}$. The study of different cases, whose details can be found in Appendix B, leads to the following incremental equations[2]:

- If $\dot{\overline{\varepsilon}}_{11} \geq 0$:
  - If $\overline{\sigma}_{11} - \overline{\sigma}_{22} \leq \left(1 - \dfrac{\widetilde{C}_{1122}}{\widetilde{C}_{1111}}\right)\overline{\sigma}^{(+)} + \widetilde{\varepsilon}_{p,22}\left(\widetilde{C}_{2222} + \widetilde{C}_{2233} - \dfrac{2\widetilde{C}_{1122}^2}{\widetilde{C}_{1111}}\right)$:
  $$\begin{cases} \dot{\varepsilon}_{p,11}^{(1)} = 0 \\ \dot{\varepsilon}_{p,11}^{(2)} = 0. \end{cases} \tag{37}$$
  - If $\left(1 - \dfrac{\widetilde{C}_{1122}}{\widetilde{C}_{1111}}\right)\overline{\sigma}^{(+)} + \widetilde{\varepsilon}_{p,22}\left(\widetilde{C}_{2222} + \widetilde{C}_{2233} - \dfrac{2\widetilde{C}_{1122}^2}{\widetilde{C}_{1111}}\right) < \overline{\sigma}_{11} - \overline{\sigma}_{22} < \langle\sigma_Y\rangle$:
  $$\begin{cases} \dot{\varepsilon}_{p,11}^{(1)} = \alpha^{(1)}\dot{\varepsilon}_{11}^{(1)} = \alpha^{(1)}\beta^{(1)}\dot{\overline{\varepsilon}}_{11} \\ \dot{\varepsilon}_{p,11}^{(2)} = 0 \\ \beta^{(1)} = \left(f_1 + f_2\dfrac{C_{1111}^{(1)} + \left(C_{1122}^{(1)} - C_{1111}^{(1)}\right)\alpha^{(1)}}{C_{1111}^{(2)}}\right)^{-1}. \end{cases} \tag{38}$$
- If $\dot{\overline{\varepsilon}}_{11} < 0$:

[2] The results are presented in the case where phase (1) reaches plasticity before phase (2) (the results for phase (2) plastifying first being just a matter of index swapping).

- If $\sigma_{11}-\sigma_{22} \geq \left(1-\frac{\widetilde{C}_{1122}}{\widetilde{C}_{1111}}\right)\overline{\sigma}^{(-)}+\widetilde{\varepsilon}_{p,22}\left(\widetilde{C}_{2222}+\widetilde{C}_{2233}-\frac{2\widetilde{C}_{1122}^2}{\widetilde{C}_{1111}}\right)$:

$$\begin{cases}\dot{\varepsilon}_{p,11}^{(1)}=0\\ \dot{\varepsilon}_{p,11}^{(2)}=0.\end{cases} \tag{39}$$

- If $\left(1-\frac{\widetilde{C}_{1122}}{\widetilde{C}_{1111}}\right)\overline{\sigma}^{(-)}+\widetilde{\varepsilon}_{p,22}\left(\widetilde{C}_{2222}+\widetilde{C}_{2233}-\frac{2\widetilde{C}_{1122}^2}{\widetilde{C}_{1111}}\right) > \overline{\sigma}_{11}-\overline{\sigma}_{22} > -\langle\sigma_Y\rangle$:

$$\begin{cases}\dot{\varepsilon}_p^{(1)}=\alpha^{(1)}\dot{\varepsilon}_{11}^{(1)}=\alpha^{(1)}\beta^{(1)}\dot{\overline{\varepsilon}}_{11}\\ \dot{\varepsilon}_p^{(2)}=0\\ \beta^{(1)}=\left(f_1+f_2\dfrac{C_{1111}^{(1)}+\left(C_{1122}^{(1)}-C_{1111}^{(1)}\right)\alpha^{(1)}}{C_{1111}^{(2)}}\right)^{-1}.\end{cases} \tag{40}$$

- If $\overline{\sigma}_{11}-\overline{\sigma}_{22}=\langle\sigma_Y\rangle$ (regardless of the sign of $\dot{\overline{\varepsilon}}_{11}$):

$$\begin{cases}\dot{\varepsilon}_{p,11}^{(1)}=\alpha^{(1)}\dot{\varepsilon}_{11}^{(1)}=\alpha^{(1)}\beta^{(1)}\dot{\overline{\varepsilon}}_{11}\\ \dot{\varepsilon}_{p,11}^{(2)}=\alpha^{(2)}\dot{\varepsilon}_{11}^{(2)}=\alpha^{(2)}\beta^{(2)}\dot{\overline{\varepsilon}}_{11}\\ \beta^{(1)}=\left(f_1+f_2\dfrac{C_{1111}^{(1)}+\left(C_{1122}^{(1)}-C_{1111}^{(1)}\right)\alpha^{(1)}}{C_{1111}^{(2)}+\left(C_{1122}^{(2)}-C_{1111}^{(2)}\right)\alpha^{(2)}}\right)^{-1}\\ \beta^{(2)}=\left(f_2+f_1\dfrac{C_{1111}^{(2)}+\left(C_{1122}^{(2)}-C_{1111}^{(2)}\right)\alpha^{(2)}}{C_{1111}^{(1)}+\left(C_{1122}^{(1)}-C_{1111}^{(1)}\right)\alpha^{(1)}}\right)^{-1}.\end{cases} \tag{41}$$

It should be noted that introducing two elastic perfectly plastic phases with different properties results in macroscopic behavior exhibiting an apparent linear (kinematic) hardening. Indeed, the local plastic flow depends on the value of the macroscopic stress, which causes the phases to reach plasticity separately. In particular, each component of the macroscopic stress tensor depends linearly (with a slope depending on the local material properties) on the macroscopic axial strain when only one phase is plastic. In the case of both local phases having reached plasticity, the macroscopic behavior becomes elastic perfectly plastic.

The incremental HEM-based elasto-plastic model has been mainly derived to take into account the effect of the microstructure on the effective properties. However, it can also be used to estimate the local plastic strains in the different phases. Indeed, the local plastic strains $\varepsilon_p^{(i)}$ are internal parameters on the HEM-based model since they are used to compute the overall plastic properties. Moreover, their evolution equation can be directly related to the macroscopic axial stress increment $\dot{\overline{\sigma}}_{11}$:

$$\dot{\overline{\sigma}}_{11}=\left(\frac{C_{1111}^{(i)}}{\alpha^{(i)}}+C_{1122}^{(i)}-C_{1111}^{(i)}\right)\dot{\varepsilon}_{p,11}^{(i)}. \tag{42}$$

The HEM-based model, combined with the wave propagation equation, can be thus used to determine (approximately) the local plastic strains in the phases without having to resort to a full-field simulations in which the local phases need to be finely meshed. In Eq. (42), the increment of local plastic strain only depends on the increment of axial stress (which is uniform in the quasi-static laminate) and the mechanical properties of the chosen phase. As such, the computation of the local plastic strain is not different from a homogeneous case.

A key point in the previous developments is that the local phases have an elastic perfectly plastic behavior. Thanks to this hypothesis, the coefficients $\alpha^{(i)}$ from Eq. (34) are constant, and the local plastic strains increments depend explicitly on the local total strain increments. Considering a strain rate dependent plasticity model would make the $\alpha^{(i)}$ functions of the plastic strains, and the plastic wave velocities would not be constant. Therefore, in the case of strain rate dependent plasticity model, a radial return algorithm would be necessary to solve the plasticity criterion, which would make the HEM model only semi-analytic.

## 4. Numerical simulation of shock wave propagation in heterogeneous elasto-plastic layered specimens

### 4.1. Numerical implementation

We will now detail the numerical methods used to solve the elasto-plastic wave propagation Eq. (13). The finite volume methods are a good choice for such problem, because they allow the use of a variety of numerical schemes suitable for hyperbolic equations (Leveque, 2002). Let us subdivide the spatial and temporal domains with constant spatial and time increments, $\Delta x$ and $\Delta t$ respectively. In non-linear wave propagation problems, explicit time integration methods are generally preferred over implicit methods because they do not require matrix inversion operations. The numerical stability of explicit methods needs to be enforced using the standard Courant–Friedrichs–Lewy (CFL) condition

$$\mathrm{CFL}=c_{\max}\frac{\Delta t}{\Delta x}\leq 1. \tag{43}$$

Eq. (43) ensures that no information propagates outside the numerical domain in which the equation is solved. The quantity $c_{max}$ is the maximum value of the axial wave velocity for all the phases considered. This enforces the validity of Eq. (43) for each spatial cell of the numerical domain. The CFL value is thus an input parameter of the simulations. The time increment $\Delta t$ is then deduced using the value of $\Delta x$ chosen and the material parameters of the phases, which allows the computation of $c_{max}$ with Eq. (15).

The quality of numerical schemes can be assessed by the amount of spurious oscillations and artificial viscosity introduced in the solution. To that extent, high resolution Godunov-type schemes offer very good performances as they introduce very little spurious oscillations and artificial viscosity (Heuzé, 2017, 2019; Leveque, 1997), compared to other method such as the Lax–Wendroff scheme, Lax–Friedrichs scheme (whose details can be found in Leveque, 1997), and the finite elements solver coupled with explicit time integration (Park et al., 2011, 2012; Mirbagheri et al., 2015; Noh and Bathe, 2013). The Godunov scheme makes notably use of a spectral decomposition of the matrix $\boldsymbol{A}$ of Eq. (13) and a flux limiter (in this case, a scalar function limiting the amplitude of the in and out-going fluxes at each cell if they are above a certain value). Thus, this method adds only a small amount of artificial viscosity locally where it is necessary, to prevent the emergence of spurious oscillations. Some illustrative examples of several numerical schemes are provided in Appendix C.

### 4.2. Description of the simulations

In this section, we describe the simulations that will be performed to study the effect of microstructural heterogeneity on elasto-plastic stress wave propagation. In order to characterize this effect, we need to consider several microstructures with various degrees of heterogeneity. We will consider the same volume fraction for the two phases ($f_1 = f_2 = 0.5$) and several couples $(\kappa^{(1)},\kappa^{(2)})$ and $(\mu^{(1)},\mu^{(2)})$ defining the stiffness tensor (4), that lead to the *same effective elastic properties*: this permits to study the sole effect of elastic heterogeneity (the yield stress being assumed to the same in both phase). Three cases will thus be considered numerically:

- The heterogeneous microstructure, comprising many elastic perfectly plastic isotropic layers, solved with the full field numerical scheme presented above.

**Table 1**
Values of the material parameters considered for the simulations.

| Test cases | $\kappa^{(1)}$ (GPa) | $\kappa^{(2)}$ (GPa) | $\mu^{(1)}$ (GPa) | $\mu^{(2)}$ (GPa) | $\rho$ (kg m$^{-3}$) | $\sigma_Y$ (MPa) | $d_{\ln}$ |
|---|---|---|---|---|---|---|---|
| Homogeneous | 175 | 175 | 80.8 | 80.8 | 7800 | 870 | 0 |
| Cases with uniform $\mu$ | | | | | | | |
| Test case 1 | 193.9 | 158.3 | 80.8 | 80.8 | 7800 | 870 | 0.2 |
| Test case 2 | 204.3 | 150.8 | 80.8 | 80.8 | 7800 | 870 | 0.3 |
| Test case 3 | 215.0 | 143.8 | 80.8 | 80.8 | 7800 | 870 | 0.4 |
| Test case 4 | 226.5 | 137.3 | 80.8 | 80.8 | 7800 | 870 | 0.5 |
| Cases with uniform $\kappa$ | | | | | | | |
| Test case 5 | 175 | 175 | 84.5 | 77.1 | 7800 | 870 | 0.2 |
| Test case 6 | 175 | 175 | 86.3 | 75.4 | 7800 | 870 | 0.3 |
| Test case 7 | 175 | 175 | 88.1 | 73.7 | 7800 | 870 | 0.4 |
| Test case 8 | 175 | 175 | 90.0 | 71.9 | 7800 | 870 | 0.5 |

- The homogenized equivalent medium (HEM) whose effective behavior is given in the incremental elasto-plastic homogenization procedure indicated in Section 3.
- A standard homogeneous isotropic description of the material in several cases: (i) with the properties of phase 1, (ii) with the properties of phase 2 and (iii) with similar elastic properties and yield stress as the HEM.

In order to characterize the mechanical contrast within the considered laminate structure, we need the have some measure of the distance between the behavior of the two phases. This can be performed using the so-called log-Euclidean distance for tensors which is invariant upon inversion and thus is suitable for elasticity tensors (Moakher and Norris, 2006; Morin et al., 2020). For two isotropic elasticity tensors (as considered here), it can be shown that the log-Euclidean distance, denoted by $d_{\ln}$, reduces to

$$d_{\ln} = \left\| \ln\left(\mathbb{C}^{(1)}\right) - \ln\left(\mathbb{C}^{(2)}\right) \right\| = \sqrt{\ln^2\left(\frac{\kappa^{(1)}}{\kappa^{(2)}}\right) + 5\ln^2\left(\frac{\mu^{(1)}}{\mu^{(2)}}\right)}. \tag{44}$$

Interestingly, the distance between the two phases is directly related to the contrast between the phases $\kappa^{(1)}/\kappa^{(2)}$ and $\mu^{(1)}/\mu^{(2)}$. Several cases will be investigated, keeping one of the parameters $\mu$ or $\kappa$ constant and varying the other one, and for various contrasts of phases. It must be noted that we do not consider any contrast in the density $\rho$ nor in the yield strength $\sigma_Y$, for sake of simplicity. As for the target behavior, we consider a behavior similar to a 12Cr steel, following Ballard (1991). The choice of this material allows the use of Hooke's law for the elastic behavior, instead of an equation of state, for applied pressure below 17 GPa. A summary of all the cases considered is given in Table 1. All the cases listed lead to the same effective elastic behavior defined by $\widetilde{\mu} = 80.8$ GPa and $\widetilde{\kappa} = 175$ GPa.

A spatial domain of length $L = 3.5$ mm is considered and it is discretized with 1800 equidistant cells, the spatial increment is thus about $\Delta x = 1.94$ μm. A CFL equal to 0.9 was considered in all simulations. The duration of the simulation is set to $T = 570$ ns, so that the stress waves can propagate long enough to be attenuated and not induce plastic strains anymore, but also so that there is no reflection at the imposed free edge at $x_1 = L$ (a second passage of the wave with an opposite sign would possibly modify the plastic strain field). Thus, all the results for the plastic strain fields will be presented at time $t = T$. The boundary conditions considered are as follows:

$$\sigma_{11}(0,t) = \begin{cases} P(t) \text{ if } t \leq 200 \text{ ns} \\ 0 \text{ if } t > 200 \text{ ns} \end{cases},$$
$$\sigma_{11}(L,t) = 0, \quad \begin{cases} v_1(x_1,0) = 0 \\ \sigma_{11}(x_1,0) = 0 \end{cases} \quad \text{for } 0 \leq x_1 \leq L, \tag{45}$$

where $P(t)$ is the applied pressure produced by the laser shock whose profile is represented in Figure 1b. The amplitude chosen will be 5 GPa[3] and the temporal duration of this signal at mid-height is about 20 ns. A free edge is enforced at $x_1 = L$. The number of layers will be set to 300 along the domain's length, i.e. each layer has a thickness of 11.7 μm. The number of spatial cells per layer is set to 6. This number of layers will ensure that the stress wave propagates through a sufficient number of layers. When considering the velocity within the homogeneous specimen in the axial direction, the stress wave spreads over 10 layers during the pulse duration. According to Ballard (1991), the limit value of the applied pressure above which hydrodynamic effects cannot be neglected is approximated by $0.1\kappa$. Therefore, the hydrodynamic effect can be neglected for all the test cases in Table 1.

### 4.3. Full-field results for the laminate

Let us first begin with an illustrative example which will be enlightening to understand the effect of material heterogeneity on the mechanical fields. The axial plastic strain profile is represented in Fig. 3 at the end of the simulation, for the test case 1, as well as the solutions for two homogeneous specimens, respectively with the properties of the phases 1 and 2 of the present test case. This last point aims to illustrate how the response of a heterogeneous microstructure is different from a homogeneous material. The plastic strain profile for the layered specimen is typical of what can be obtained with the full field model. In particular, the profile exhibits sharp variations whose lengths correspond to the thickness of the layers, corresponding to discontinuities from one phase to another. This "oscillatory" plastic strain profile is thus a consequence of the heterogeneous elastic behavior of the laminate. When comparing it to the response of the two homogeneous specimens, it clearly appears that adopting a layered description drastically changes the behavior of the specimen. Except for the initial part of the profiles ($x_1 \leq 0.4$ mm, approximately), the behaviors of the phases are neither bounds for the variations of the full field solution, nor a correct match for the affected depth, i.e. the depth up to which plastic strains are non zero. This is due to the fact that the shockwave is damped when plastifying the specimen, and to the fact that a mechanical interaction arises between both phases in the laminate, modifying the local stress state. However at some point in the laminate, the value of the stress wave is not high enough to plastify one of the phase. It is then only damped in only one of them (the other behaving elastically), allowing it to travel further without being completely attenuated to the lowest value necessary to plastify at least one phase. In the homogeneous cases, the wave is continuously attenuated, hence the shorter affected depth.

Since the response of the heterogeneous specimen shows an oscillatory behavior, the study of its mean behavior is also of interest to characterize the effect of the heterogeneity. This mean behavior can be

[3] Though the results will be presented for a positive amplitude, the interpretations are also valid for a negative amplitude, which would correspond better to LSP applications.

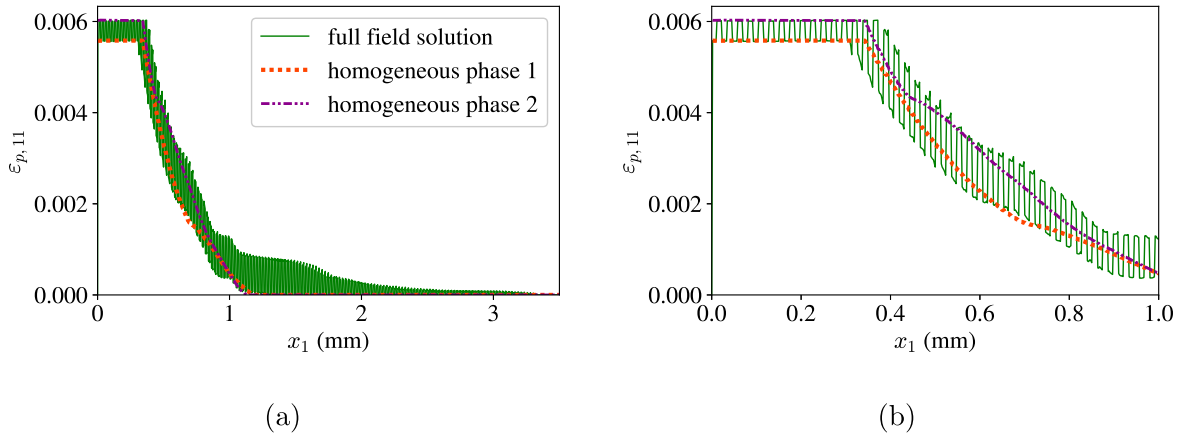


**Fig. 3.** Comparison of the plastic strain profiles for the heterogeneous case, the homogeneous case with elastic properties $(\kappa^{(1)}, \mu^{(1)})$ and the homogeneous case with elastic properties $(\kappa^{(2)}, \mu^{(2)})$. (a) Representation in the entire spatial domain and (b) Enlarged view to show the oscillatory nature of the profile in the laminate specimen.

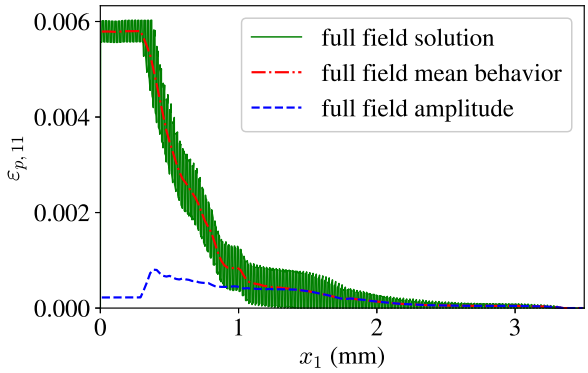


**Fig. 4.** Distribution of the post-treated mean behavior and amplitude profiles calculated from the full field solution of the laminate in the test case 1.

easily computed from the full oscillatory profile, as a post-treatment, by averaging the values at the layers' interfaces. The amplitude of the plastic strain variations are also computed from the response shown in Fig. 3. The associated post-treated mean behavior as well as the amplitude of the variations are represented in Fig. 4 for illustrative purposes.

The influence of the material parameters $\kappa^{(1)}$, $\kappa^{(2)}$, $\mu^{(1)}$ and $\mu^{(2)}$ on the mean behavior of the plastic strain and on the amplitude of its variations are now investigated and shown in Figs. 5 and 6. In the case of the mean behavior, the comparisons will include the homogeneous specimen (with elastic properties $\widetilde{\mu} = 80.8$ GPa and $\widetilde{\kappa} = 175$ GPa), which does not exhibit variations in the solution, to emphasize how the behaviors deviate from it.

The results of Figs. 5a and 6a show that the mean behavior of all test cases differs significantly from the homogeneous specimen, even for a small value of the elastic contrast, indicating the presence of an apparent hardening. More precisely, in all cases, the mean behaviors correspond at first to the homogeneous specimen, but some differences are observed at depths $x_1 \geq 1$ mm, resulting in a greater depth affected by plastic strains. However this new affected depth does not seem to vary with the elastic parameters. When a plastic stress wave propagates through the specimen, it is gradually attenuated until its amplitude is no longer high enough for plasticity to be active. The fact that the affected depth does not vary with the elastic contrast indicates that the stress waves reach the same distance before being completely attenuated down to the lowest value of the axial stress causing the phases to reach plasticity.

As for the amplitudes of the variations in Figs. 5b and 6b, they increase with the elastic contrast between the phases. As the latter increases, the amount of plasticity induced in the layer with the higher value of $\kappa$ or $\mu$ will decrease, since this layer is becoming stiffer, while it will increase in the other, which results in an increase of the variations amplitude.

### *4.4. Local plastic strain heterogeneities predicted by the HEM-based modeling*

We will now present the results of the HEM-based plasticity model developed in Section 3.3. As explained in this section, the HEM-based model contains several internal parameters involved in the definition of the macroscopic fields. In particular, the local plastic strain field is known and reduces to the sole variables $\varepsilon^{(1)}_{p,11}$ and $\varepsilon^{(2)}_{p,11}$ since the local plastic strain field is uniform within the two phases. Thus, in the simulations performed with the HEM-based model, the local plastic strain *at each node of the domain* in the two phases can be estimated. As shown in Section 3, this estimation relies on the assumption that the laminate is subjected to macroscopically homogeneous boundary conditions, at each node of the domain.

We will now compare those plastic strains per phase calculated from the HEM-based model with the local plastic strain obtained with the full-field procedure. The plastic strain profiles are compared in Fig. 7 for the test cases 1 and 5, and in Fig. 8 for the test cases 4 and 8.

It is remarkable to note that the plastic strain profiles in the phases, determined from the HEM-based model, define almost perfectly the envelope of the oscillatory distribution of plastic strain obtained with the reference full-field procedure. Such a match is actually observed in all test cases. A possible explanation is that this HEM model is the exact solution for a quasi-static loading, and that its extension to a dynamic loading such as one with a wavelength high enough compared to the thickness of the layers is still a good approximation. One can also notice that the plastic strain profiles for phase 1 and 2 do not present the same behavior when $\kappa$ or $\mu$ is taken constant: the phases with the higher plastic strain values are swapped between the two profiles in Figs. 7b and 8b once the plastic strain stops saturating (and starts diminishing). This feature is in agreement with the results of the full-field solution for which this 'crossing' is also observed (see the sudden decrease of the plastic strain amplitude in Fig. 6b at $x_1 \simeq 0.3$ mm). Those results imply that the HEM-based model succeeds in reproducing the amplitude of the variations.

### *4.5. Mean plastic strain estimated by the HEM-based model*

The HEM-based model allows computing the effective axial plastic strain $\widetilde{\varepsilon}_{p,11}$. However, as addressed in Section 3.3, the effective axial

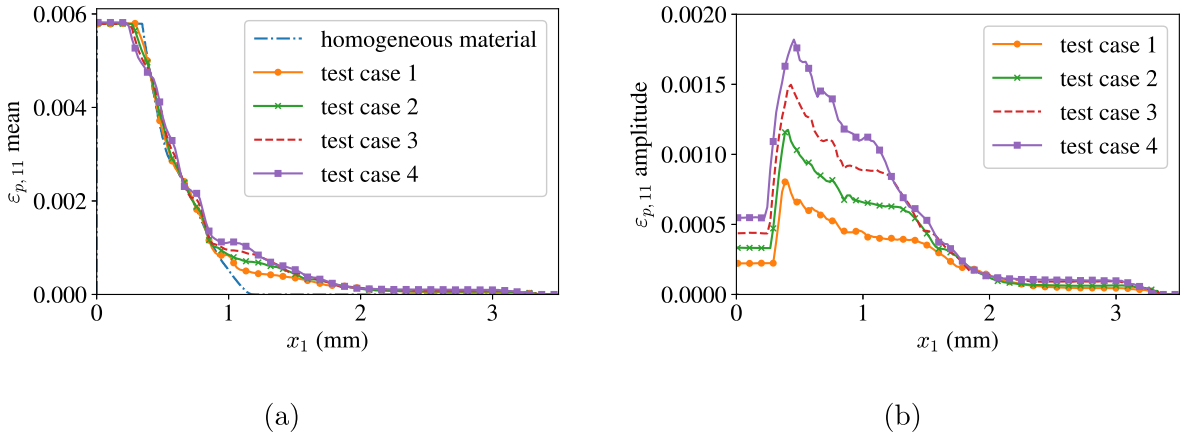


**Fig. 5.** Influence of the heterogeneity of the moduli $\kappa^{(i)}$ (with constant coefficient $\mu$) on the distribution of the plastic strain (cases 1 to 4). (a) Mean plastic strain and (b) Amplitude of variations of the plastic strain field.

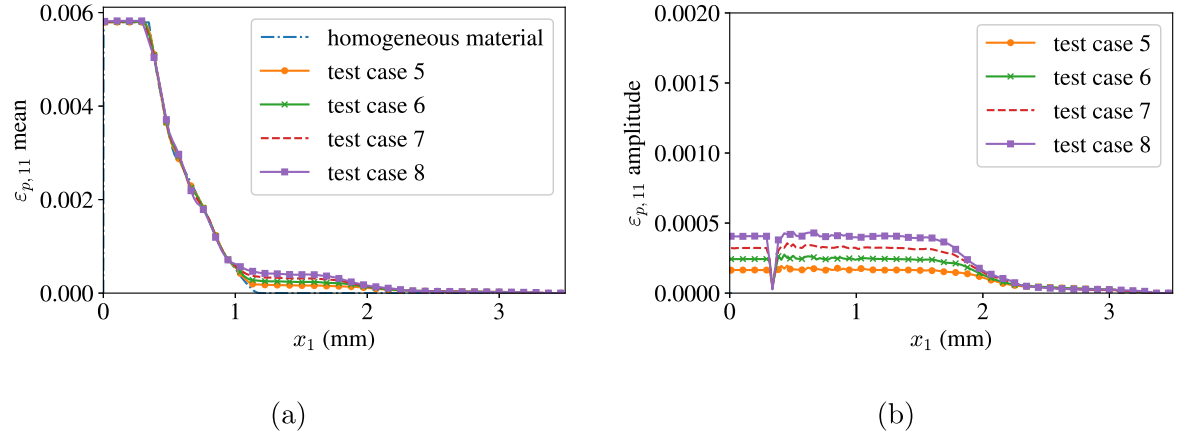


**Fig. 6.** Influence of the heterogeneity of the moduli $\mu^{(i)}$ (with constant coefficient $\kappa$) on the distribution of the plastic strain (cases 5 to 8). (a) Mean plastic strain and (b) Amplitude of variations of the plastic strain field.

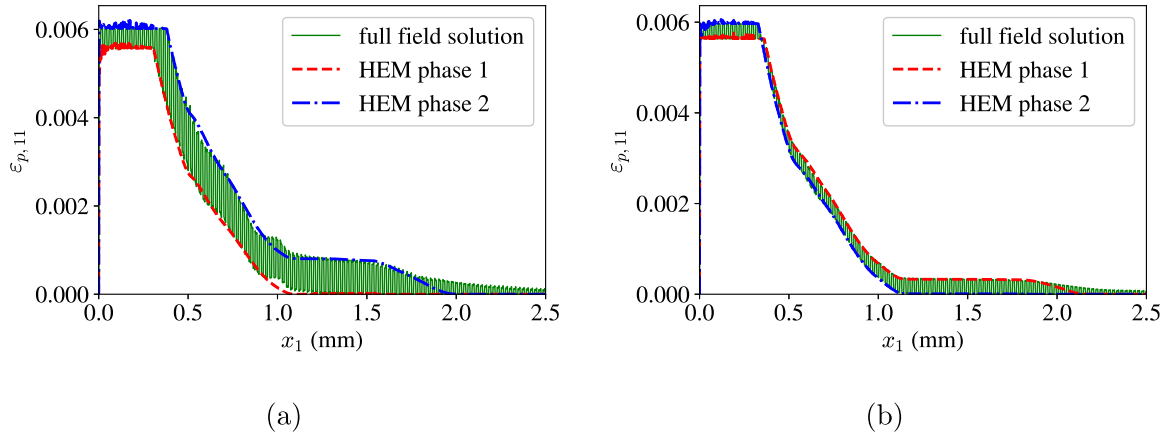


**Fig. 7.** Superposition of the full field plastic strain profile and the local plastic strain obtained using the HEM. (a) Test case 1 and (b) test case 5.

plastic strain $\widetilde{\varepsilon}_{p,11}$ is not equal to the mean axial plastic strain defined by $\langle \varepsilon_{p,11} \rangle$. On the other hand, in the full field simulations, it is the quantity $\langle \varepsilon_{p,11} \rangle$ that is computed from the envelope of the variations and displayed in Figs. 5a and 6a. Thus, to further assess the performance of the HEM-based model, the *mean axial plastic strain* will be considered instead of the effective axial plastic strain for the comparison with the full-field solution. It can be also remarked that, as an indication, in the considered cases, the deviation between the mean plastic strain and the effective plastic strain predicted by the HEM-based model is always less that 3.7%.

The profiles of mean plastic strain are represented in Fig. 9 for the cases 1 and 5 (with both $d_{\ln} = 0.2$) and in Fig. 10 for the cases 4 and 8 (with both $d_{\ln} = 0.5$).

From Figs. 9 and 10 we can see that there is a good agreement between the mean plastic strain of the HEM-based model and the mean plastic strain calculated using the numerical full-field approach.

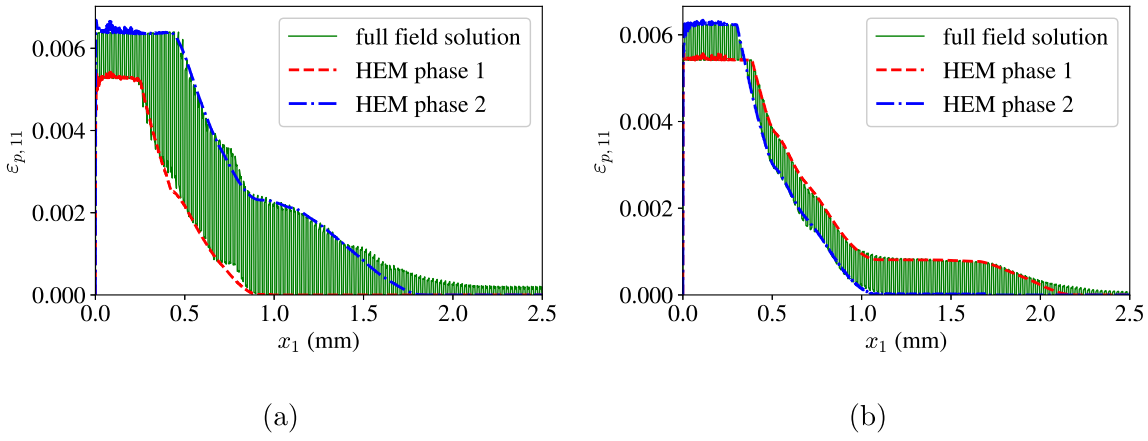


**Fig. 8.** Superposition of the full field plastic strain profile and the local plastic strain obtained using the HEM. (a) Test case 4 and (b) test case 8.

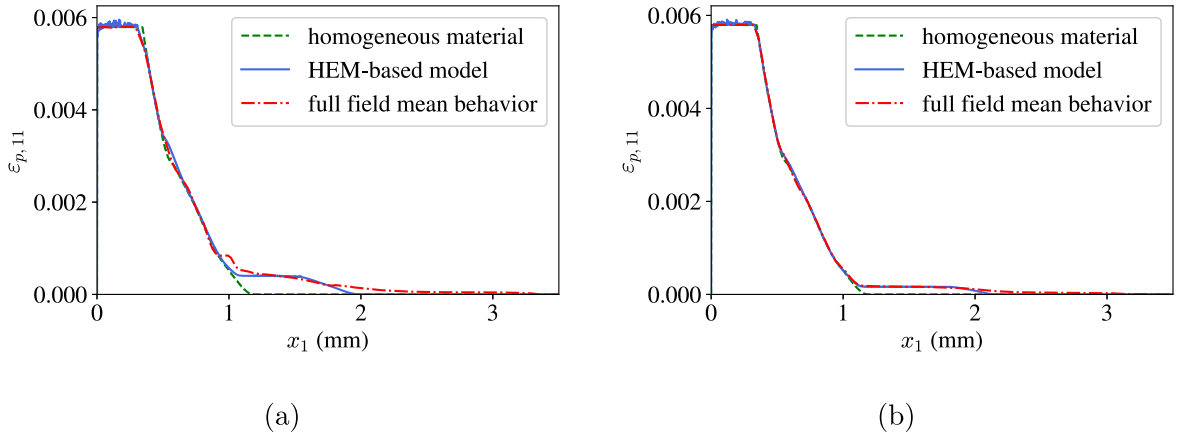


**Fig. 9.** Comparison between the mean plastic strain of the HEM-based model and the mean plastic strain of the full field reference solution for $d_{\text{In}} = 0.2$. (a) Test case 1 (a) and (b) Test case 5.

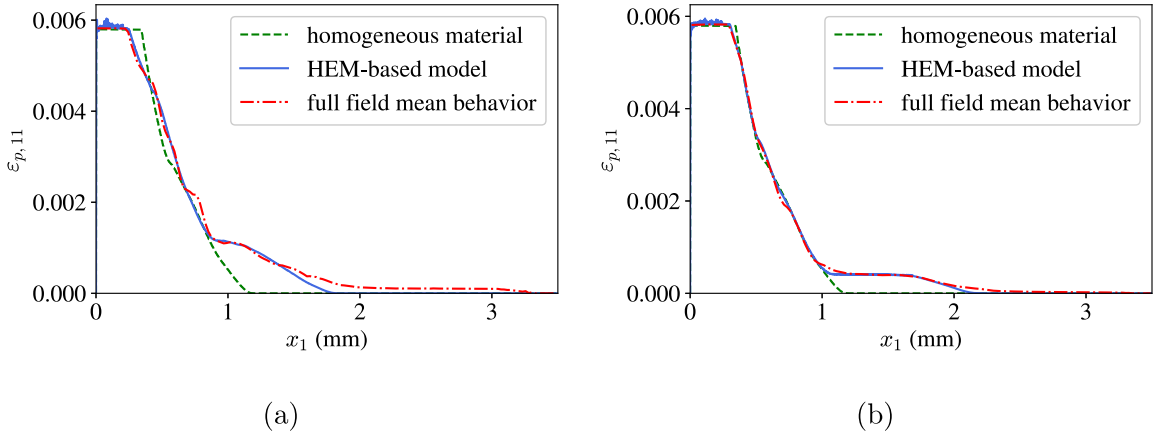


**Fig. 10.** Comparison between the mean plastic strain of the HEM-based model and the mean plastic strain of the full-field solution for $d_{\text{In}} = 0.5$. (a) Test case 4 (a) and (b) Test case 8.

When considering the microstructure heterogeneity, the depth affected by LSP, in which plastic strain occurs, is about twice as large as the one predicted by the standard approach in which the specimen is supposed to be homogeneous. The comparison with the homogeneous behavior illustrates the important impact of the mechanical heterogeneities. Figs. 9 and 10 show that the use the HEM-based model, which is composed of three evolution domains (the two phases are elastic, one is plastic and both are plastic), each with an associated incremental law, allows the reproduction, on average, of the correct solution provided by the full field procedure to a good accuracy. In particular, the comparison holds particularly well in the case where $\kappa$ remains constant between the phases (Figs. 9b and 10b), which is related to the low level of the variations amplitude as shown in Fig. 6b.

In Figs. 9 and 10, and particularly in Figs. 9a and 10a, the affected depth predicted by the HEM-based model is slightly lower than the affected depth predicted by the reference full-field procedure. This

difference can be related to the presence of reflections of the stress wave in the laminate specimen due to the impedance mismatch which are absent in the HEM-based model. In the full-field solution, after a certain time, the stress wave is damped to the lowest value of axial stress needed to trigger plasticity in at least one phase. However, because of the reflections, this value may be exceeded by a little amount, thus inducing a small amount of plastic strain at a depth where the stress wave in the HEM model has been attenuated enough not to generate plastic strains. Such a difference in the predictions, also displayed in Figs. 7 and 8, may have repercussions on the residual stresses prediction. However, the plastically affected depth does not a priori correspond to the depth to which residual stresses are introduced. The residual stresses can be non zero where there is no plastic strain, since the material must be at equilibrium. Further work is required to investigate deeply the link between the distribution of plastic strain in the heterogeneous material and the build up of the residual stress field.

### 4.6. Comments on the loading conditions

It should be noted that, in the present simulations, the applied maximum stress was equal to 5 GPa, which is always higher than $2\sigma_{\mathrm{HEL}}$ with

$$\sigma_{\mathrm{HEL}} = \sigma_Y \left( \frac{2}{3} + \frac{\kappa}{2\mu} \right). \tag{46}$$

The quantity $\sigma_{\mathrm{HEL}}$ defined in (46) is called the Hugoniot Elastic Limit. Thus, for this applied loading, the plastic strain saturates (in the first part of the domain), as it can be observed in the form of a 'plateau' in Figs. 3, 4, 5, 6, 9 and 10. As explained in Ballard (1991), in an isotropic homogeneous material, the plastic strain in these parts does not depend of the amplitude $P$ of the pressure but only on the material parameters. The hypotheses leading to the derivation of the expression of this saturated plastic strain are also valid at the local scale in the full-field and HEM model, since the local phases are homogeneous isotropic, with incompressible plasticity. It can thus be notably shown that, if the pressure has an amplitude greater than $2\sigma_{\mathrm{HEL}}$ (which is the case here), the value of the saturation plateau in the phases, denoted by $\epsilon_p^{max}$ is given by

$$\epsilon_p^{max,(i)} = \frac{2C_{1111}^{(i)}\sigma_Y^{(i)}}{\left(C_{1111}^{(i)} - C_{1122}^{(i)}\right)\left(C_{1111}^{(i)} + 2C_{1122}^{(i)}\right)} = \frac{1}{3}\left(\frac{1}{\mu^{(i)}} + \frac{4}{3\kappa^{(i)}}\right)\sigma_Y^{(i)}. \tag{47}$$

The validity of (47) for the local plastic strain computed by the HEM-based model can be verified in Figs. 7 and 8. Its validity for a homogeneous or heterogeneous case is also numerically verified by the fact that the saturation plateaus are identical between the heterogeneous full-field solution, and homogeneous solutions in Fig. 3. Thus when the value of $\kappa$ or $\mu$ increases, the value of $\epsilon_p^{max}$ decreases, as verified in Figs. 8a and 8b. It is also interesting to note that, when $\sigma_{\mathrm{HEL}}$ decreases, the affected depth increases. The affected depth should thus increase when $\kappa$ decreases or when $\mu$ increases, as it is also verified in Figs. 8a and 8b.

It must be noted that the choice of the loading amplitude $P$ was arbitrary, and a value under the threshold $2\sigma_{\mathrm{HEL}}$ would have given different plastic strain profiles, without however changing the conclusions drawn from the present study, concerning the greater affected depth, the profiles of the mean plastic strain of the full-field solution, and the increase of the amplitudes with the elastic contrast.

## 5. Discussion

The numerical simulations of a laser shock propagating in an heterogeneous specimen have permitted to show interesting features on the residual plastic strain related to the elastic heterogeneity between the phases. Indeed, the plastic strain profile exhibits discontinuities at the phases' interfaces. From this profile, the mean plastic strain and the amplitude of its variations have been extracted in order to characterize the effect of the contrast in the elastic behavior between the two phases. An increase of the elastic contrast leads to an increase of the amplitude of the variations and modify the plastic strain distribution. In LSP, the plastic strain profile induced by the elasto-plastic wave propagation results in the emergence of residual stresses which are expected to increase fatigue resistance. Thus, the heterogeneity of the plastic strain profile described in this work can have important consequences upon the fatigue resistance as it induces heterogeneous residual stresses at the scale of the individual components of the microstructure.

The effect of heterogeneity has also been studied by means of a HEM-based model accounting for the heterogeneous microstructure. A quasi-static elasto-plastic homogenization has been performed and lead to a macroscopic elasto-plastic with internal parameter describing the local conditions of plasticity of the phase. For each domain, incremental laws are derived, to allow the computation of the stress wave propagation as well as the update of the internal variables. As a result, the outcome of the model is the mean plastic behavior of the microstructure but also an estimate of the localized plastic strains in the phases. The predictions of the HEM-based model have been compared to the reference numerical results of provided by the full-field procedure and a very good agreement was observed: the HEM-based model captures very accurately the mean plastic profile as well as the envelope of the variations amplitudes. Such results have promising consequences in terms of computational costs. Indeed, the main drawback of the full-field simulations is that they require a very fine spatial discretization in order to describe each layer. Thus for large specimen with small heterogeneities, the computation time can become prohibitive. In contrast, the HEM-based model does not require particularly fine mesh and can be an appealing alternative to estimate the fluctuation of the plastic strain in heterogeneous specimens subjected to a laser shock. More generally, such an approach will allow accounting for the specific microstructure of the metallic specimen treated by LSP, such as the average grain shape and the crystallographic texture, and the associated anisotropic elasto-visco-plastic behavior. This requires using a homogenization model adapted to such microstructures, as in Castelnau et al. (2001), Blackman et al. (2017) and Gu et al. (2019). It is thus possible to approximate closely the features of the full-field solution with a HEM-based model requiring far less computation time. As an indication, *for the test case 4* of Table 1, the time required by the HEM-based model is approximately five times less than the time required by the full-field simulation to achieve comparable results. A more thorough study is however necessary to draw definitive conclusions. The minimum computation time required by the full field model to achieve converged results depends on the number of layers, since each layer has to be meshed finely enough. Thus the computation time gained by the use of the HEM-based model depends on the number of layers of the microstructure, and is expected to increase as the number of layers increases. The mechanical properties also influence the computational resources necessary, since Eq. (43) must hold. It means that for a given $\Delta x$ and CFL number, the higher the elastic velocity, the lower the time increment will be, and the computation will thus require more increments to finish.

Finally, we also want to emphasize that the results obtained with the HEM-based model are only valid for heterogeneities with small characteristic size compared to the wavelength of the dynamic loading, as explained in Capdeville et al. (2010). Indeed, for thick layers, replacing the specimen comprising a small number of thick layers by its HEM is not a valid procedure. To illustrate this, let us consider again the test case 4 of Table 1, with the same simulation parameters as in the previous simulations but only 20 layers are considered, so their thickness is now 0.175 mm. The distribution of the plastic strain, represented in Fig. 11 shows that the results for the HEM-based model do not match with the reference full-field solution, due to the low number of layers. The difficulty arising from such an observation is to

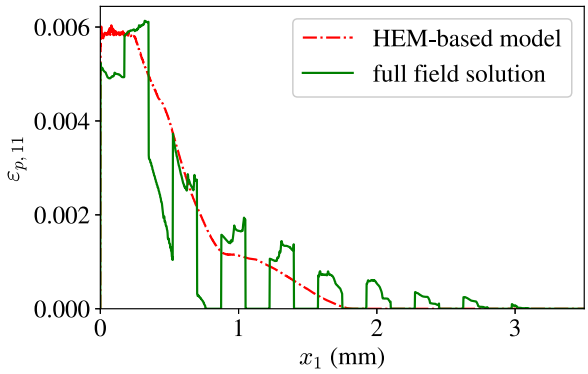


**Fig. 11.** Plastic strain profiles for the full-field and HEM-based models in the case of thick layers.

clearly identify the number of layers, for a given loading and material, above which one can safely use the HEM-based model to approximate the full-field behavior.

As an indication, different simulations of the test case 4 but with different numbers of layers show that the overall difference between the mean plastic strain computed with the full-field and HEM-based models significantly decreases up to 250 layers, and then seems to reach a plateau. We stress that a more thorough study is necessary to draw definitive conclusions.

## 6. Conclusion

The present work aimed at providing an improved modeling of a laser impact on a metallic specimen, by taking into account the specimen's microstructure. We considered the simplified case of a laminate microstructure subjected to a uniaxial state of strain. The microstructure was composed of two phases alternating periodically and perfectly bonded together. Following those hypotheses, we modeled the stress wave propagation via an hyperbolic PDE system, which we solve using a high-resolution Godunov scheme. To further describe the effect of the laminate microstructure on the stress wave propagation but at a lower numerical cost, an elasto-plastic HEM-based model has been developed. This HEM-based model is found to be able to reproduce accurately the spatial distribution of the mean plastic strain within the specimen compared to the reference full-field numerical solution, provided the number of layers is high enough. More significantly, this HEM-based elasto-plastic model allows to compute the local plastic strains in the phases (without however knowing their precise position within the sample), which permits to estimate the magnitude of the residual plastic strain heterogeneities. The advantage of the HEM-based model is that it permits to decrease the computational time since it does not require to mesh finely each layer, in contrast with the full-field approach. With this simplified model, the CPU gain is about a factor 6 but we anticipate that it will become significantly larger when dealing with 2D or even 3D cases and when considering more complex microstructures such as the ones of polycrystalline materials (Quey et al., 2011; Eghtesad et al., 2018).

The present results constitute a first step towards the simulation of micro-LSP, for which the effect of the microstructure heterogeneity is expected to be important. Some further developments are needed in the following directions:

- Only two different phases were considered for the laminate specimen. It would be interesting to extend the developments to a larger number of phases.
- An experimental validation of the results is necessary to properly assess the effect of the microstructure in the residual plastic strain. Co-laminated metallic specimens produced by accumulative roll bonding (ARB) would be good candidates to assess the model as the number and thickness of the layers can be finely controlled (Verstraete et al., 2018).
- The current works paves the way for further developments including a description of the microstructure of a polycrystal aggregates comprising anisotropic grains with different orientations, resulting in different material properties along the direction of the shock. Contrary to the present work, these microstructures would also have some degree of randomness in their description.
- The extension of the present work to a 2D or 3D case (e.g. with a polycrystalline microstructure) is necessary in order to provide distributions of residual stresses which are ultimately of interest to study the possible increase of fatigue life after laser shock peening.
- Only the plastic strain fields in heterogeneous materials have been investigated in the present work. The prediction of the associated residual stress field (using e.g. eigenstrain methods) would be of important practical interest for LSP applications. In that regard, comparisons with 2D or 3D FEM calculations of residual stresses will permit to assess the 1D model.

## Declaration of competing interest

The authors declare that they have no known competing financial interests or personal relationships that could have appeared to influence the work reported in this paper.

## Acknowledgment

This research was partly funded by the Carnot Institute ARTS and by the French Agence Nationale de la Recherche (ANR), research project ForgeLaser (grant number: ANR-18-CE08-0026).

## Appendix A. Effective stiffness tensor $\widetilde{\mathbb{C}}$

We give here the details about the derivation of the effective stiffness tensor $\widetilde{\mathbb{C}}$ for the purely elastic two-phase laminate. The proof is based on the developments and results of Postma (1955) and Milton (2002), but given in the more general case of phases with transverse isotropic behavior:

$$\mathbb{C} = \begin{pmatrix} C_{1111} & C_{1122} & C_{1122} & 0 & 0 & 0 \\ C_{1122} & C_{2222} & C_{2233} & 0 & 0 & 0 \\ C_{1122} & C_{2233} & C_{2222} & 0 & 0 & 0 \\ 0 & 0 & 0 & 2C_{2323} & 0 & 0 \\ 0 & 0 & 0 & 0 & 2C_{1313} & 0 \\ 0 & 0 & 0 & 0 & 0 & 2C_{1313} \end{pmatrix}, \tag{A.1}$$

with $2C_{2323} = C_{2222} - C_{2233}$. Let us first express the non-uniform diagonal components of the mechanical fields:

$$\begin{cases} \varepsilon_{e,11} = \dfrac{\sigma_{11}}{C_{1111}} - \dfrac{C_{1122}}{C_{1111}}\varepsilon_{e,22} - \dfrac{C_{1122}}{C_{1111}}\varepsilon_{e,33} \\ \sigma_{22} = C_{1122}\varepsilon_{e,11} + C_{2222}\varepsilon_{e,22} + C_{2233}\varepsilon_{e,33} \\ \sigma_{33} = C_{1122}\varepsilon_{e,11} + C_{2233}\varepsilon_{e,22} + C_{2222}\varepsilon_{e,33}. \end{cases} \tag{A.2}$$

System (A.2) is then written alternatively by injecting the first equation of the system into the other two, and by identifying the uniform quantities (given by Eq. (25)):

$$\begin{cases} \varepsilon_{e,11} = \dfrac{\overline{\sigma}_{11}}{C_{1111}} - \dfrac{C_{1122}}{C_{1111}}\overline{\varepsilon}_{e,22} - \dfrac{C_{1122}}{C_{1111}}\overline{\varepsilon}_{e,33} \\ \sigma_{22} = \dfrac{C_{1122}}{C_{1111}}\overline{\sigma}_{11} + \left(C_{2222} - \dfrac{(C_{1122})^2}{C_{1111}}\right)\overline{\varepsilon}_{e,22} + \left(C_{2233} - \dfrac{(C_{1122})^2}{C_{1111}}\right)\overline{\varepsilon}_{e,33} \\ \sigma_{33} = \dfrac{C_{1122}}{C_{1111}}\overline{\sigma}_{11} + \left(C_{2233} - \dfrac{(C_{1122})^2}{C_{1111}}\right)\overline{\varepsilon}_{e,22} + \left(C_{2222} - \dfrac{(C_{1122})^2}{C_{1111}}\right)\overline{\varepsilon}_{e,33}. \end{cases}$$

(A.3)

By taking the spatial average in system (A.3), one gets:

$$\begin{cases} \overline{\varepsilon}_{e,11} = \langle \varepsilon_{e,11} \rangle = \left\langle \frac{1}{C_{1111}} \right\rangle \overline{\sigma}_{11} - \left\langle \frac{C_{1122}}{C_{1111}} \right\rangle \overline{\varepsilon}_{e,22} - \left\langle \frac{C_{1122}}{C_{1111}} \right\rangle \overline{\varepsilon}_{e,33} \\ \overline{\sigma}_{22} = \langle \sigma_{22} \rangle = \left\langle \frac{C_{1122}}{C_{1111}} \right\rangle \overline{\sigma}_{11} + \left( \langle C_{2222} \rangle - \left\langle \frac{(C_{1122})^2}{C_{1111}} \right\rangle \right) \overline{\varepsilon}_{e,22} \\ + \left( \langle C_{2233} \rangle - \left\langle \frac{(C_{1122})^2}{C_{1111}} \right\rangle \right) \overline{\varepsilon}_{e,33} \\ \overline{\sigma}_{33} = \langle \sigma_{33} \rangle = \left\langle \frac{C_{1122}}{C_{1111}} \right\rangle \overline{\sigma}_{11} + \left( \langle C_{2233} \rangle - \left\langle \frac{(C_{1122})^2}{C_{1111}} \right\rangle \right) \overline{\varepsilon}_{e,22} \\ + \left( \langle C_{2222} \rangle - \left\langle \frac{(C_{1122})^2}{C_{1111}} \right\rangle \right) \overline{\varepsilon}_{e,33}. \end{cases} \tag{A.4}$$

This leads to the expressions of the components $\widetilde{C}_{1111}$, $\widetilde{C}_{2222}$, $\widetilde{C}_{1122}$ and $\widetilde{C}_{2233}$ of the effective stiffness tensor:

$$\begin{aligned} \widetilde{C}_{1111} &= \left\langle \frac{1}{C_{1111}} \right\rangle^{-1}, \\ \widetilde{C}_{2222} &= \langle C_{2222} \rangle + \left\langle \frac{1}{C_{1111}} \right\rangle^{-1} \left\langle \frac{C_{1122}}{C_{1111}} \right\rangle^2 - \left\langle \frac{(C_{1122})^2}{C_{1111}} \right\rangle, \\ \widetilde{C}_{1122} &= \left\langle \frac{1}{C_{1111}} \right\rangle^{-1} \left\langle \frac{C_{1122}}{C_{1111}} \right\rangle, \\ \widetilde{C}_{2233} &= \langle C_{2233} \rangle + \left\langle \frac{1}{C_{1111}} \right\rangle^{-1} \left\langle \frac{C_{1122}}{C_{1111}} \right\rangle^2 - \left\langle \frac{(C_{1122})^2}{C_{1111}} \right\rangle. \end{aligned} \tag{A.5}$$

The determination of the shear coefficients of the effective stiffness tensor follows a similar reasoning. Let us first express the non-uniform off-diagonal components of the mechanical fields (in terms of the uniform components):

$$\begin{cases} \varepsilon_{e,13} = \dfrac{\overline{\sigma}_{13}}{C_{1313}} \\ \varepsilon_{e,12} = \dfrac{\overline{\sigma}_{12}}{C_{1313}} \\ \sigma_{23} = C_{2323} \overline{\varepsilon}_{e,23}. \end{cases} \tag{A.6}$$

By taking the spatial average in system (A.6), one gets the expressions of $\widetilde{C}_{1212}$, $\widetilde{C}_{1313}$ and $\widetilde{C}_{2323}$:

$$\widetilde{C}_{1212} = \widetilde{C}_{1313} = \left\langle \frac{1}{C_{1313}} \right\rangle^{-1}, \quad \widetilde{C}_{2323} = \langle C_{2323} \rangle. \tag{A.7}$$

Since $2C_{2323} = C_{2222} - C_{2233}$, one also has $2\widetilde{C}_{2323} = \widetilde{C}_{2222} - \widetilde{C}_{2233}$.

The isotropic case considered in this work is achieved by using the results of this appendix with $C_{2233} = C_{1122}$, $C_{2222} = C_{1111}$ and $C_{2323} = C_{1313}$.

## Appendix B. Effective plasticity model

We now detail the developments leading to the determination of the conditions on the macroscopic stress $\overline{\sigma}$ for which the local phases reach plasticity, given by Eqs. (37)–(41). It must be noted that only the value of $\overline{\sigma}_{11}$ is required to assess local plasticity, but the conditions will be given in terms of $\overline{\sigma}_{11} - \overline{\sigma}_{22}$ in order to define a macroscopic criterion whose structure follows the local plasticity criterion (11). Those derivations lead to closed-form expressions.

### *B.1. One phase has reached plasticity*

We start by deriving the expressions of the coefficients $\beta^{(i)}$ used in Eqs. (38) and (40). The developments will be made in the case of phase 1 reaching plasticity before phase 2. We start from the definition of $\dot{\overline{\varepsilon}}_{11}$:

$$\dot{\overline{\varepsilon}}_{11} = f_1 \dot{\varepsilon}_{11}^{(1)} + f_2 \dot{\varepsilon}_{11}^{(2)}. \tag{B.1}$$

By taking advantage of the uniformity of the axial stress and the definition of the coefficient $\alpha$ defined in Eq. (17), we can express $\dot{\varepsilon}_{11}^{(2)}$ as a function of $\dot{\varepsilon}_{11}^{(1)}$

$$\dot{\varepsilon}_{11}^{(2)} = \frac{C_{1111}^{(1)} \left(1 - \alpha^{(1)}\right) + \alpha^{(1)} C_{1122}^{(1)}}{C_{1111}^{(2)}} \dot{\varepsilon}_{11}^{(1)}. \tag{B.2}$$

Substituting (B.2) in (B.1), one gets

$$\dot{\varepsilon}_{11}^{(1)} = \left( f_1 + f_2 \frac{C_{1111}^{(1)} + \left(C_{1122}^{(1)} - C_{1111}^{(1)}\right) \alpha^{(1)}}{C_{1111}^{(2)}} \right)^{-1} \dot{\overline{\varepsilon}}_{11} = \beta^{(1)} \dot{\overline{\varepsilon}}_{11}. \tag{B.3}$$

Still considering that phase 1 reaches plasticity before phase 2, the expression of $\beta^{(2)}$ is:

$$\beta^{(2)} = \left( f_2 + f_1 \frac{C_{1111}^{(2)}}{C_{1111}^{(1)} + \left(C_{1122}^{(1)} - C_{1111}^{(1)}\right) \alpha^{(1)}} \right)^{-1}. \tag{B.4}$$

*Loading path characterized by* $\dot{\overline{\varepsilon}}_{11} > 0$. In order to assess the macroscopic stress state for which the evolution becomes plastic, one needs to study the local plasticity criterion; the local plasticity criterion $(1)_4$ reduces to:

$$\left(1 - \frac{C_{1122}}{C_{1111}}\right) \sigma_{11} + \left( \frac{(C_{1122})^2}{C_{1111}} - \frac{C_{2222} + C_{2233}}{2} \right) \epsilon_{p,11} = \sigma_Y. \tag{B.5}$$

Since $\sigma_{11}$ is uniform in the laminate (i.e. $\sigma_{11} = \overline{\sigma}_{11}$), on can deduce the value of $\overline{\sigma}_{11}$ for which local plasticity occurs, denoted by $\overline{\sigma}^{(+)}$:

$$\overline{\sigma}^{(+)} = \min_{(i)} \left( \frac{C_{1111}^{(i)}}{C_{1111}^{(i)} - C_{1122}^{(i)}} \left[ \sigma_Y^{(i)} - \left( \frac{(C_{1122}^{(i)})^2}{C_{1111}^{(i)}} - \frac{C_{2222}^{(i)} + C_{2233}^{(i)}}{2} \right) \epsilon_{p,11}^{(i)} \right] \right). \tag{B.6}$$

The evolution remains elastic as long as $\overline{\sigma}_{11} \leq \overline{\sigma}^{(+)}$, i.e. as long as:

$$\overline{\sigma}_{11} - \overline{\sigma}_{22} \leq \left(1 - \frac{\widetilde{C}_{1122}}{\widetilde{C}_{1111}}\right) \overline{\sigma}^{(+)} + \widetilde{\varepsilon}_{p,22} \left( \widetilde{C}_{2222} + \widetilde{C}_{2233} - \frac{2\widetilde{C}_{1122}^2}{\widetilde{C}_{1111}} \right). \tag{B.7}$$

*Loading path characterized by* $\dot{\overline{\varepsilon}}_{11} < 0$. In that case, the local plasticity criterion is met when

$$\left(1 - \frac{C_{1122}}{C_{1111}}\right) \sigma_{11} + \left( \frac{(C_{1122})^2}{C_{1111}} - \frac{C_{2222} + C_{2233}}{2} \right) \epsilon_{p,11} = -\sigma_Y. \tag{B.8}$$

The minus sign of the right-hand side indicates a compression evolution, or an unloading from a tension state of stress. The value of $\overline{\sigma}_{11}$ for which one of the phase reaches plasticity, denoted by $\overline{\sigma}^{(-)}$, is given by:

$$\overline{\sigma}^{(-)} = \max_{(i)} \left( \frac{C_{1111}^{(i)}}{C_{1111}^{(i)} - C_{1122}^{(i)}} \left[ -\sigma_Y^{(i)} - \left( \frac{(C_{1122}^{(i)})^2}{C_{1111}^{(i)}} - \frac{C_{2222}^{(i)} + C_{2233}^{(i)}}{2} \right) \epsilon_{p,11}^{(i)} \right] \right). \tag{B.9}$$

The evolution remains elastic as long as $\overline{\sigma}_{11} \geq \overline{\sigma}^{(-)}$, which translates to the following condition on $\overline{\sigma}_{11} - \overline{\sigma}_{22}$:

$$\overline{\sigma}_{11} - \overline{\sigma}_{22} \geq \left(1 - \frac{\widetilde{C}_{1122}}{\widetilde{C}_{1111}}\right) \overline{\sigma}^{(-)} + \widetilde{\varepsilon}_{p,22} \left( \widetilde{C}_{2222} + \widetilde{C}_{2233} - \frac{2\widetilde{C}_{1122}^2}{\widetilde{C}_{1111}} \right). \tag{B.10}$$

### *B.2. All phases have reached plasticity*

We start again by deriving the expressions of the $\beta^{(i)}$, used this time in Eq. (41). The developments are similar to the previous case, but here all the $\dot{\varepsilon}_{p,11}^{(i)}$ are non zero. Since both phases are plastic, the expression of $\beta^{(2)}$ can be found from $\beta^{(1)}$ by swapping indexes. Let us first express $\dot{\varepsilon}_{11}^{(2)}$ as a function of $\dot{\varepsilon}_{11}^{(1)}$:

$$\dot{\varepsilon}_{11}^{(2)} = \frac{C_{1111}^{(1)} + \left(C_{1122}^{(1)} - C_{1111}^{(1)}\right) \alpha^{(1)}}{C_{1111}^{(2)} + \left(C_{1122}^{(2)} - C_{1111}^{(2)}\right) \alpha^{(2)}} \dot{\varepsilon}_{11}^{(1)}. \tag{B.11}$$

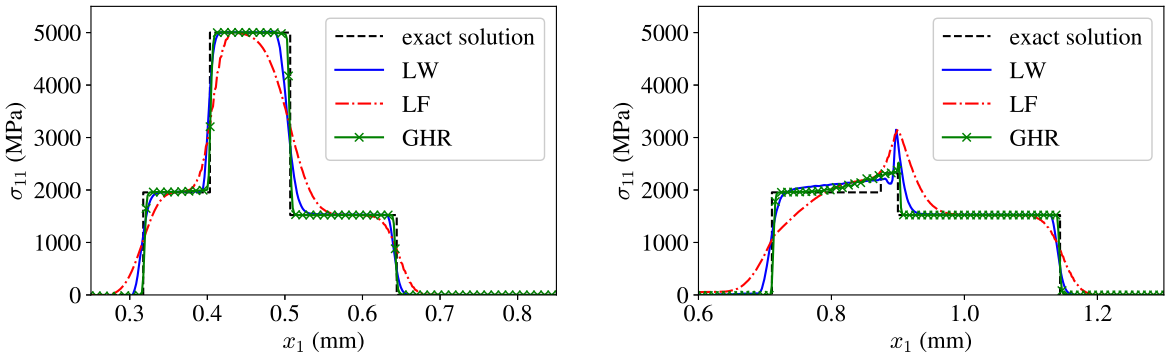


**Fig. C.1.** Comparison of the different numerical schemes for a square loading (LW: Lax–Wendroff, LF: Lax–Friedrichs, GHR: Godunov High Resolution). (a) Snapshot $t = 107$ ns and (b) Snapshot $t = 190$ ns.

This leads to the expression of $\beta^{(1)}$:

$$\dot{\varepsilon}_{11}^{(1)} = \left( f_1 + f_2 \frac{C_{1111}^{(1)} + \left(C_{1122}^{(1)} - C_{1111}^{(1)}\right)\alpha^{(1)}}{C_{1111}^{(2)} + \left(C_{1122}^{(2)} - C_{1111}^{(2)}\right)\alpha^{(2)}} \right)^{-1} \dot{\bar{\varepsilon}}_{11} = \beta^{(1)} \dot{\bar{\varepsilon}}_{11} \tag{B.12}$$

Then, we derive the value of $|\bar{\sigma}_{11} - \bar{\sigma}_{22}|$ when all phases have reached plasticity. (Here the absolute value is useful since the developments are valid whether the specimen is in a compression or tension state of stress). With Eq. (32) and the expression of $\widetilde{\varepsilon}_{p,22}$ given in (33), $|\bar{\sigma}_{11} - \bar{\sigma}_{22}|$ is given by:

$$|\bar{\sigma}_{11} - \bar{\sigma}_{22}| = \left| \left(1 - \frac{\widetilde{C}_{1122}}{\widetilde{C}_{1111}}\right)\bar{\sigma}_{11} - \widetilde{C}_{1122} M_2 \right|. \tag{B.13}$$

Let $\hat{\bar{\sigma}}$ denote the axial stress $\sigma_{11}$ such that all phases have reached plasticity. The value of the local plastic strain induced by such an axial stress can be derived from the local plasticity criterion (B.5) in each phases:

$$\hat{\varepsilon}_p = \frac{2C_{1111}}{2(C_{1122})^2 - C_{1111}(C_{2222} + C_{2233})} \left( \pm\sigma_Y - \left(1 - \frac{C_{1122}}{C_{1111}}\right)\hat{\bar{\sigma}} \right). \tag{B.14}$$

The symbol $\pm$ denotes the fact that we do not draw a distinction on whether both phases reach plasticity for a compression or tension state of stress. Now using Eq. (31), the value of $M_2$ can be deduced:

$$M_2 = \frac{1}{\widetilde{C}_{1122}} \left[ f_1 \left( \left(1 - \frac{C_{1122}^{(1)}}{C_{1111}^{(1)}}\right)\hat{\bar{\sigma}} - \left(\pm\sigma_Y^{(1)}\right) \right) + f_2 \left( \left(1 - \frac{C_{1122}^{(2)}}{C_{1111}^{(2)}}\right)\hat{\bar{\sigma}} - \left(\pm\sigma_Y^{(2)}\right) \right) \right]. \tag{B.15}$$

Eq. (B.13) thus reduces to:

$$|\bar{\sigma}_{11} - \bar{\sigma}_{22}| = \left| \hat{\bar{\sigma}} \left( 1 - \frac{\widetilde{C}_{1122}}{\widetilde{C}_{1111}} - f_1 \left(1 - \frac{C_{1122}^{(1)}}{C_{1111}^{(1)}}\right) - f_2 \left(1 - \frac{C_{1122}^{(2)}}{C_{1111}^{(2)}}\right) \right) + f_1 \left(\pm\sigma_Y^{(1)}\right) + f_2 \left(\pm\sigma_Y^{(2)}\right) \right|. \tag{B.16}$$

From the definition of $\widetilde{C}_{1111}$ and $\widetilde{C}_{1122}$, one has

$$\frac{\widetilde{C}_{1122}}{\widetilde{C}_{1111}} = \left\langle \frac{C_{1122}}{C_{1111}} \right\rangle, \tag{B.17}$$

and, by taking advantage of the relation $f_1 + f_2 = 1$, it is straightforward to see that

$$1 - \frac{\widetilde{C}_{1122}}{\widetilde{C}_{1111}} - f_1 \left(1 - \frac{C_{1122}^{(1)}}{C_{1111}^{(1)}}\right) - f_2 \left(1 - \frac{C_{1122}^{(2)}}{C_{1111}^{(2)}}\right) = 0. \tag{B.18}$$

The condition on the macroscopic stress is thus given by:

$$|\bar{\sigma}_{11} - \bar{\sigma}_{22}| = \left| f_1 \left(\pm\sigma_Y^{(1)}\right) + f_2 \left(\pm\sigma_Y^{(2)}\right) \right| = \langle \sigma_Y \rangle. \tag{B.19}$$

This condition implies that the macroscopic equivalent stress is equal to the mean yield strength when all the phases have reached plasticity.

## Appendix C. Numerical methods comparison

In order to assess the accuracy of Godunov high resolution scheme considered in this work, we compare its predictions with other standard schemes of the literature (Lax–Friedrich and Lax–Wendroff) in a model problem of a square stress loading, with an amplitude of 5 GPa for a duration of 40 ns, propagating in an homogeneous isotropic material (with $E = 210$ GPa, $\nu = 0.3$, $\rho = 7800$ kg m$^{-3}$ and $\sigma_Y = 870$ MPa). This problem admits an analytical solution which can be easily determined by the method of characteristics (Ballard, 1991). The spatial domain considered for the comparison has a length of $L = 2.2$ mm, subdivided in 1200 elements (enough to reach convergence). The quantity $c\Delta t/\Delta x$ in Eq. (43) is set to 0.9.

The distribution of the axial stress $\sigma_{11}$ is represented in Fig. C.1 at the snapshots at $t = 107$ ns and $t = 190$ ns. One can see that the Lax–Friedrichs scheme adds too much viscosity to the solution, since the sharp variations are not well captured. The solution is improved with the Lax–Wendroff scheme, but some spurious oscillations are present as well as some artificial viscosity. Among the numerical schemes considered, the Godunov high resolution scheme appears to be the most suitable method as it is closer to the analytical solution, which is in agreement with previous works (Heuzé, 2017).

## References


Agrawal, V., Bhattacharya, K., 2014. Shock wave propagation through a model one dimensional heterogeneous medium. Int. J. Solids Struct. 51, 3604–3618.

Ballard, P., 1991. Contraintes Résiduelles Induites par Impact Rapide. Application au Choc Laser (Ph.D. Thesis). Ecole Polytechnique.

Berezovski, A., Berezovski, M., Engelbrecht, J., 2006. Numerical simulation of nonlinear elastic wave propagation in piecewise homogeneous media. Mater. Sci. Eng. A 364–369.

Blackman, D., Boyce, D., Castelnau, O., Dawson, P., Laske, G., 2017. Effects of crystal preferred orientation on upper-mantle flow near plate boundaries: rheologic feedbacks and seismic anisotropy. Geophys. J. Int. 210, 1481–1493.

Braisted, W., 1999. Finite element simulation of laser shock peening. Int. J. Fatigue 21, 719–724.

Brockman, R.A., Braisted, W.R., Olson, S.E., Tenaglia, R.D., Clauer, A.H., Langer, K., Shepard, M.J., 2012. Prediction and characterization of residual stresses from laser shock peening. Int. J. Fatigue 36, 96–108.

Capdeville, Y., Guillot, L., Marigo, J.J., 2010. 1-d non-periodic homogenization for the seismic wave equation. Geophys. J. Int. 897–910.

Capdeville, Y., Marigo, J.J., 2007. Second order homogenization of the elastic wave equation for non-periodic layered media. Geophys. J. Int. 170, 823–838.

Castelnau, O., Francillette, H., Bacroix, B., Lebensohn, R., 2001. Texture dependent plastic behavior of Zr 702 at large strain. J. Nucl. Mater. 297, 14–26.

Chaieb, I., 2004. Analyse et Simulation des Contraintes Résiduelles Induites par des Traitements Mécaniques de Précontrainte en Grenaillage et Choc Laser (Ph.D. Thesis). Université de Reims Champagne-Ardenne.

Chatzigeorgiou, G., Charalambakis, N., Murat, F., 2009. Homogenization of a pressurized tube made of elastoplastic materials with discontinuous properties. Int. J. Solids Struct. 46, 3902–3913.

Chen, X., Chandra, N., 2004. The effect of heterogeneity on plane wave propagation through layered composites. Compos. Sci. Technol. 64, 1477–1493.

Chen, X., Chandra, N., Rajendran, A., 2004. Analytical solution to the plate impact problem of layered heterogeneous material systems. Int. J. Solids Struct. 41, 4635–4659.

Clauer, A.H., 2019. Laser shock peening, the path to production. Metals 9, 626.

Ding, K., Ye, L., 2006. Laser Shock Peening Performance and Process Simulation. Woodhead Publishing Limited.

Eghtesad, A., Barrett, T.J., Knezevic, M., 2018. Compact reconstruction of orientation distributions using generalized spherical harmonics to advance large-scale crystal plasticity modeling: Verification using cubic, hexagonal, and orthorhombic polycrystals. Acta Mater. 155, 418–432.

Fabbro, R., Fournier, J., Ballard, P., Devaux, D., Virmont, J., 1990. Physical study of laser-produced plasma in confined geometry. J. Appl. Phys. 68, 775–784.

Fox, J.A., 1974. Effect of water and paint coatings on laser-irradiated targets. Appl. Phys. Lett. 24, 461–464.

Gu, T., Medy, J.R., Klosek, V., Castelnau, O., Forest, S., Hervé-Luanco, F., Proudhon, H., Renault, P.O., Thilly, L., Villechaise, P., 2019. Multiscale modeling of the elastoplastic behavior of architectured and nanostructured Cu-Nb composite wires and comparison with neutron diffraction experiments. Int. J. Plast. 122, 1–30.

He, Q.C., Feng, Z.Q., 2012. Homogenization of layered elastoplastic composites: Theoretical results. Int. J. Non-Linear Mech. 47, 367–376.

Heuzé, T., 2017. Lax–Wendroff and TVD finite volume methods for unidimensional thermomechanical numerical simulations of impacts on elastic–plastic solids. J. Comput. Phys. 346, 369–388.

Heuzé, T., 2019. Lax-Wendroff schemes for elastic–plastic solids. J. Comput. Phys. 396, 89–105.

Johnson, G.R., Cook, W.H., 1983. A constitutive model and data for metals subjected to large strains, high strain rates and high temperatures. In: Proceedings 7th International Symposium on Ballistics, pp. 541–547.

Le Bras, C., Rondepierre, A., Seddik, R., Scius-Bertrand, M., Rouchausse, Y., Videau, L., Fayolle, B., Gervais, M., Morin, L., Valadon, S., Ecault, R., Furfari, D., Berthe, L., 2019. Laser shock peening: Toward the use of pliable solid polymers for confinement. Metals 9, 793.

Leveque, R.J., 1997. Wave propagation algorithms for multidimensional hyperbolic systems. J. Comput. Phys. 131, 327–353.

Leveque, R.J., 2002. Finite Volume Methods for Hyperbolic Problems. Cambridge university press edition.

Milton, G.W., 2002. The Theory of Composites. In: Cambridge monographs on applied and computational mathematics edition.

Mirbagheri, Y., Nahvi, H., Parvizian, J., Düster, 2015. Reducing spurious oscillations in discontinuous wave propagation simulation using high-order finite elements. Comput. Math. Appl. 70, 1640–1658.

Moakher, M., Norris, A.N., 2006. The closest elastic tensor of arbitrary symmetry to an elasticity tensor of lower symmetry. J. Elasticity 85, 215–263.

Montross, C., Wei, T., Ye, L., Clark, G., Mai, Y.W., 2002. Laser shock processing and its effects on microstructure and properties of metal alloys: a review. Int. J. Fatigue 24, 1021–1036.

Morin, L., Gilormini, P., Derrien, K., 2020. Generalized euclidean distances for elasticity tensors. J. Elasticity 138, 221–232.

Noh, G., Bathe, K.J., 2013. An explicit time integration scheme for the analysis of wave propagations. Comput. Struct. 129, 178–193.

Park, K.C., Lim, S.J., Huh, H., 2011. An Explicit Integration Method for Analysis of Wave Propagation in Heterogeneous Materials. In: Mechanics of Solids, Structures and Fluids; Vibration, Acoustics and Wave Propagation, Vol. 8, ASMEDC, Denver, Colorado, USA, pp. 547–555.

Park, K.C., Lim, S.J., Huh, H., 2012. A method for computation of discontinuous wave propagation in heterogeneous solids: basic algorithm description and application to one-dimensional problems. Internat. J. Numer. Methods Engrg. 91, 622–643.

Peyre, P., Berthe, L., Scherpereel, X., Fabbro, R., 1998. Laser-shock processing of aluminium-coated 55c1 steel in water-confinement regime, characterization and application to high-cycle fatigue behaviour. J. Mater. Sci. 1421–1429.

Peyre, P., Berthe, L., Vignal, V., Popa, I., Baudin, T., 2012. Analysis of laser shock waves and resulting surface deformations in an Al–Cu–Li aluminum alloy. J. Phys. D: Appl. Phys. 45, 335304.

Peyre, P., Chaieb, I., Braham, C., 2007. FEM Calculation of residual stresses induced by laser shock processing in stainless steels. Modelling Simulation Mater. Sci. Eng. 15, 205–221.

Peyre, P., Fabbro, R., Merrien, P., Lieurade, H., 1996. Laser shock processing of aluminium alloys. Application to high cycle fatigue behaviour. Mater. Sci. Eng. A 210, 102–113.

Peyre, P., Sollier, A., Chaieb, I., Berthe, L., Bartnicki, E., Braham, C., Fabbro, R., 2003. FEM Simulation of residual stresses induced by laser Peening. Eur. Phys. J. Appl. Phys. 23, 83–88.

Postma, G.W., 1955. Wave propagation in a stratified medium. Geophysics 20, 27.

Quey, R., Dawson, P., Barbe, F., 2011. Large-scale 3D random polycrystals for the finite element method: Generation, meshing and remeshing. Comput. Methods Appl. Mech. Engrg. 200, 1729–1745.

Rondepierre, A., Ünaldi, S., Rouchausse, Y., Videau, L., Fabbro, R., Casagrande, O., Besaucéle, O., Berthe, L., 2021. Beam size dependency of a laser-induced plasma in confined regime: Shortening of the plasma release. Influence on pressure and thermal loading. Opt. Laser Technol. 135, 106689.

Scius-Bertrand, M., Videau, L., Rondepierre, A., Lescoute, E., Rouchausse, Y., Kaufman, J., Rostohar, D., Brajer, J., Berthe, L., 2021. Laser induced plasma characterization in direct and water confined regimes: new advances in experimental studies and numerical modelling. J. Phys. D: Appl. Phys. 54, 055204.

Seddik, R., Rondepierre, A., Prabhakaran, S., Morin, L., Favier, V., Palin-Luc, T., Berthe, L., 2021. Identification of constitutive equations at very high strain rates using shock wave produced by laser. Eur. J. Mech. A Solids 104432.

Song, H., 2010. Analyse Expérimentale et Numérique de la Distribution des Contraintes Résiduelles Induites par Choc-Laser dans les Alliages d'Aluminium (Ph.D. Thesis). Ecole Nationale Supérieure Des Arts et Métiers.

Tedesco, J.W., Landis, D.W., 1989. Wave propagation through layered systems. Comput. Struct. 32, 625–638.

Verstraete, K., Azzedine, H., Helbert, A.L., Brisset, F., Bradai, D., Baudin, T., 2018. Accumulative roll bonding at room temperature of a bi-metallic AA5754/AA6061 composite: Impact of strain path on microstructure, texture, and mechanical properties: Accumulative roll bonding at room temperature. Adv. Energy Mater. 20, 1700285.

Vukelić, S., Kysar, J.W., Yao, Y.Lawrence., 2009. Grain boundary response of aluminum bicrystal under micro scale laser shock peening. Int. J. Solids Struct. 46, 3323–3335.

Vukelic, S., Wang, Y., Kysar, J.W., Yao, Y.L., 2009. Dynamic material response of aluminum single crystal under microscale laser shock peening. J. Manuf. Sci. Eng. 131, 031015.

Wang, Y., Kysar, J.W., Yao, Y.L., 2008. Analytical solution of anisotropic plastic deformation induced by micro-scale laser shock peening. Mech. Mater. 40, 100–114.

Zhuang, S., Ravichandran, G., Grady, D.E., 2003. An experimental investigation of shock wave propagation in periodically layered composites. J. Mech. Phys. Solids 51, 245–265.